Available online at www.sciencedirect.com
SCIENCE DIRECT®
Geochimica et Cosmochimica Acta 70 (2006) 364–383
Geochimica
www.elsevier.com/locate/gca

Dissolution kinetics as a function of the Gibbs free energy of reaction: An experimental study based on albite feldspar

Roland Hellmann *, Delphine Tisserand

Fluids and Dynamics of the Crust Group, LGIT, CNRS UMR C5559, OSUG, Université Joseph Fourier, 38041 Grenoble Cedex 9, France

Received 16 May 2005; accepted in revised form 10 October 2005

Abstract

Here we report on an experimental investigation of the relation between the dissolution rate of albite feldspar and the Gibbs free energy of reaction, ΔG_r. The experiments were carried out in a continuously stirred flow-through reactor at 150 °C and $pH_{(150\ °C)}$ 9.2. The dissolution rates R are based on steady-state Si and Al concentrations and sample mass loss. The overall relation between ΔG_r and R was determined over a free energy range of $-150 < \Delta G_r < -15.6$ kJ mol^{-1}. The data define a continuous and highly non-linear, sigmoidal relation between R and ΔG_r that is characterized by three distinct free energy regions. The region furthest from equilibrium, delimited by $-150 < \Delta G_r < -70$ kJ mol^{-1}, represents an extensive dissolution rate plateau with an average rate $\overline{R} = 1.0 \times 10^{-8}$ mol m^{-2} s^{-1}. In this free energy range the rates of dissolution are constant and independent of ΔG_r, as well as [Si] and [Al]. The free energy range delimited by $-70 \leqslant \Delta G_r \leqslant -25$ kJ mol^{-1}, referred to as the 'transition equilibrium' region, is characterized by a sharp decrease in dissolution rates with increasing ΔG_r, indicating a very strong inverse dependence of the rates on free energy. Dissolution nearest equilibrium, defined by $\Delta G_r > -25$ kJ mol^{-1}, represents the 'near equilibrium' region where the rates decrease as chemical equilibrium is approached, but with a much weaker dependence on ΔG_r. The lowest rate measured in this study, $R = 6.2 \times 10^{-11}$ mol m^{-2} s^{-1} at $\Delta G_r = -16.3$ kJ mol^{-1}, is more than two orders of magnitude slower than the plateau rate. The data have been fitted to a rate equation (adapted from Burch et al. [Burch, T. E., Nagy, K. L., Lasaga, A. C., 1993. Free energy dependence of albite dissolution kinetics at 80 °C and pH 8.8. *Chem. Geol.* **105**, 137–162]) that represents the sum of two parallel reactions

$$R = k_1[1 - \exp(-ng^{m_1})] + k_2[1 - \exp(-g)]^{m_2},$$

where k_1 and k_2 are rate constants that have been determined by regression, with values 1.02×10^{-8} and 1.80×10^{-10} mol m^{-2} s^{-1}, $g \equiv |\Delta G_r|/\mathrm{R}T$ is a dimensionless number, and n, m_1, and m_2 are adjustable fitted parameters ($n = 7.98 \times 10^{-5}$, $m_1 = 3.81$ and $m_2 = 1.17$). Based on measurements of the temporal evolution of R_{Si} and R_{Al} for each experiment, steady-state dissolution rates appear to be congruent at all ΔG_r. In contrast, non-steady-state dissolution is incongruent, and is related to ΔG_r. Scanning electron microscopy (SEM) images of post-reaction grain surfaces indicate that dissolution close to equilibrium ($\Delta G_r > -25$ kJ mol^{-1}) resulted in the precipitation of a secondary crystalline phase, but there are no indications that this altered the measured R–ΔG_r relation.

1. Introduction

The chemical weathering of rocks is a process that exerts a major control on element cycling in the Earth's crust, aqueous element concentrations in the hydrological cycle, global change via the CO_2 budget, soil development, and environmental concerns at the Earth's surface. In trying to quantify and model natural chemical weathering reactions (e.g., Lasaga et al., 1994; Lasaga, 1998), geoscientists have approached the problem from three major directions: measurements in the field, generally extending from the catchment to the continental scale; laboratory experiments aimed at studying individual water–mineral reactions;

* Corresponding author.
E-mail address: hellmann@obs.ujf-grenoble.fr (R. Hellmann).

0016-7037/$ - see front matter © 2005 Elsevier Inc. All rights reserved.
doi:10.1016/j.gca.2005.10.007

computer modeling of water–mineral reactions at the microscopic scale. Laboratory experiments occupy the middle-ground between field scale measurements and molecular scale processes simulated by computer codes, and thus serve as a bridge between these two end member approaches to the study of chemical weathering.

Data derived from experimental mineral dissolution and precipitation studies are generally fit to kinetic equations that incorporate major rate-controlling parameters; two general forms (adapted from Lasaga, 1995; see also Eq. (30) in Aagaard and Helgeson, 1982) particularly useful for describing mineral dissolution are

$$R = k_0 \exp^{-E_a/RT} a_{H^+,OH^-}^{n_{H^+},n_{OH^-}} g(I) \prod_i a_i^{n_i} f(\Delta G_r), \quad (1a)$$

$$R = k_+ a_{H^+,OH^-}^{n_{H^+},n_{OH^-}} g(I) \prod_i a_i^{n_i} f(\Delta G_r). \quad (1b)$$

In Eqs. (1a) and (1b) R is the overall rate of reaction (mol m^{-2} s^{-1}); this is the quantity that is directly measured in an experiment and is most commonly based on the concentration(s) of elements released from the mineral to solution. In Eq. (1a), applicable at any temperature, the term $k_0 \exp(-E_a/RT)$ imparts the temperature dependence on the rate via the apparent activation energy of the overall reaction E_a; R and T are the gas constant and temperature (K), and k_0 is a rate constant (same units as R) that incorporates pre-exponential factors in the Arrhenius relation. At constant temperature, it is simpler to consider Eq. (1b), where the product $k_0 \exp(-E_a/RT)$ is replaced by just a single term, the forward rate constant for the overall dissolution reaction, k_+ (with units mol m^{-2} s^{-1}; note that the m^{-2} term refers to a constant surface area). Overall mineral dissolution rate equations are alternatively written to include a separate term for the (non-constant) reactive surface area that multiplies k_+; however, this changes the units of R to mol s^{-1}. The pH dependence of the rate is expressed by the a_{H^+,OH^-} term, and as written here, represents the activity of either the hydronium or hydroxyl ion raised to the corresponding exponent n (note that the value of n depends on the pH); at circum-neutral pH conditions where the rate may be independent of pH, the a_{H^+,OH^-} term can be omitted. The $g(I)$ parameter describes the dependence of the rate on ionic strength, and the $\prod_i a_i^{n_i}$ term expresses the effect of aqueous species that catalyze or inhibit the overall rate. The last term, $f(\Delta G_r)$, is a generalized function representing the Gibbs free energy of reaction that quantifies the effect of how far from chemical equilibrium the (dissolution) reaction takes place.

With respect to the kinetics of dissolution, probably no other mineral has been as extensively studied as the feldspars. The influence of pH ($a_{H^+,OH^-}^{n_{H^+},n_{OH^-}}$) and T on the dissolution rate has received the most attention (for reviews of past work see, e.g., Hellmann, 1994; Blum and Stillings, 1995). The effect of inhibitors ($\prod_i a_i^{n_i}$ term in Eqs. (1a) and (1b)), such as Al or organic ligands, which can act both as inhibitors or catalysts, has also been investigated in a number of studies; for Al, see, e.g., Chou and Wollast (1985), Oelkers et al. (1994), Oelkers (2001); for organic ligands, see e.g., Oelkers and Schott (1998), Ullman and Welch, 2002, and references therein. The relation between the dissolution rate and $f(\Delta G_r)$ has also been the subject of much recent interest and has been studied for a large number of minerals and glasses. With respect to the feldspars, we cite some recent experimental studies treating R and $f(\Delta G_r)$ (Burch et al., 1993; Oelkers et al., 1994; Gautier et al., 1994; Berger, 1995; Alekseyev et al., 1997; Murakami et al., 1998; Taylor et al., 2000; Berger et al., 2002; Beig and Lüttge, 2006, in press). Despite this relatively large number of studies, there are significant differences in the data sets. An analysis and comparison of these studies will be discussed in an upcoming study.

In the present study we investigate the influence of ΔG_r on the rate of dissolution of albite at basic pH conditions and 150 °C. The dissolution reaction can be expressed as

$$NaAlSi_3O_8 + 2H_2O \rightarrow Na^+ + Al(OH)_4^- + 3SiO_2(aq) \quad (2)$$

The goals that motivated us to carry out the present study can be summarized as follows: (a) Most past studies are based on limited ranges and/or limited continuity of R–ΔG_r data; our dissolution rates have been measured, to the best of our knowledge, over the largest and most continuous range of ΔG_r to date for any mineral. Therefore, the R–ΔG_r data from this study will be useful for quantifying and modeling water–albite (feldspar) interactions from near equilibrium all the way to far-from-equilibrium conditions, and very importantly, including the intermediate ΔG_r range where R changes rapidly and is strongly dependent on ΔG_r. (b) Our R–ΔG_r data extend all the way to $\Delta G_r = -150$ kJ mol^{-1}; this allows us for the first time to unequivocally test for the existence of an extended dissolution rate plateau (i.e., with respect to rate data based on input solutions with $[Si]_i$, $[Al]_i = 0$, or $[Si]_i : [Al]_i$ equal to mineral stoichiometry). (c) Given the fundamental differences in published R–ΔG_r data sets and their respective interpretations, our data provide new information that can be used to critically evaluate existing data and models, and potentially provide a new interpretation on the mechanism(s) of dissolution. (d) This study will further our knowledge with respect to resolving the role $f(\Delta G_r)$ plays in the significant discrepancy between field and laboratory dissolution rates.

1.1. Importance of dissolution rates and ΔG_r for feldspar

The dissolution of feldspars in many natural environments occurs at near equilibrium conditions, which indicates that a comprehensive understanding of feldspar dissolution behavior requires laboratory experiments over a large range of ΔG_r, and not just at far-from-equilibrium conditions. A compilation of selected soil water chemistries (see Table 8, Figs. 18 and 19; White, 1995) reveals that albite and K-feldspar solubilities are approached or even exceeded at circum-neutral pH. Feldspar saturation states in natural waters between 0 and

300 °C, compiled by Stefánsson and Arnórsson (2000), show that non-geothermal ground waters and surface waters range from undersaturated to saturated with respect to low and high albite, microcline, and sanidine (depending on pH), and are undersaturated at all pH with respect to anorthite. From the same study, geothermal waters at elevated temperatures (50–200 °C) are slightly supersaturated with respect to low albite and microcline, but are close to saturation with respect to high albite and sanidine. On the other hand, these same waters are undersaturated with respect to anorthite at temperatures <200 °C, and relatively close to saturation at temperatures >200 °C. Another geothermal study, based on drill core samples and fluid-rock modeling applied to the Rhein graben, and specifically at the Soultz-sous-Forêts (France) deep geothermal drilling site, confirm that albite and K-feldspar are common precipitation products at depth (Komninou and Yardley, 1997), indicating that both dissolution and precipitation processes occur under these conditions.

Theoretical studies are dependent on reaction path modeling that are used to quantitatively predict the temporal and spatial evolution of rock-water interactions. In general, simulations of water–rock interactions are based not only on equilibrium thermodynamic relations, but also on kinetic data (rate laws) concerning dissolution reactions of minerals very close to equilibrium, or precipitation reactions when fluids become supersaturated. Thus, incorporation of accurate dissolution rates and rate laws for a wide variety of minerals over a large span of ΔG_r is of critical importance for theoretical modeling studies dealing with the evolution of water–rock systems. As we will show later on, use of a conventional 'transition state' rate law at near equilibrium can result in a serious over-estimation of dissolution rates.

Interest in the relation between the free energy of reaction ΔG_r and the rate of dissolution is also due to the discrepancies between mineral dissolution rates measured in the laboratory versus the field. It is well known that estimated chemical weathering rates of minerals in the field are generally several orders of magnitude slower than corresponding rates (~25 °C) in the laboratory (e.g., Velbel, 1989, 1993; White and Brantley, 2003). As an example, in a compilation of alkali feldspar dissolution rates by White (1995), experimental rates range from −11.9 to −12.8, compared to field rates (in soils) that span −13.3 to −16.5 (log rates, mol m^{-2} s^{-1}); even slower rates (−17.7) have been estimated for K-feldspar dissolution in an aquifer (Zhu et al., 2004).

The discrepancies between field and laboratory rates are not due to any intrinsic difference in rates, but rather are caused by differences in dissolution conditions and difficulties in estimating certain rate-influencing parameters (e.g., Velbel, 1993; Swoboda-Colberg and Drever, 1993; Drever and Clow, 1995; White and Brantley, 2003). Moreover, two issues standout in importance: (a) the first is a physical parameter and is related to the difficulty of accurately assessing reactive surface area in the field (e.g., Velbel, 1989, 1993; Schnoor, 1990; Swoboda-Colberg and Drever, 1993; White, 1995). The extreme end-member case is when mineral surface areas do not contribute to dissolution due to fluid bypassing (e.g., unconnected pore spaces). (b) The second factor is chemical in nature and is based on major differences in ΔG_r between field and laboratory dissolution conditions. Reactions in natural environments are commonly assumed to occur closer to chemical equilibrium (higher free energy), with slower rates as a consequence. Moreover, field rates represent the sum of dissolution reactions occurring in different environments at different free energies. Specifically, the overall rate of chemical weathering appears to be a complicated function of the percolation rate and the physical communication between fluid-mineral interactions occurring in micropores and reactions in large channels or macropores; not only are the surface areas different in these two environments, but the fluid residence times are also vastly different, and therefore the corresponding dissolution reactions occur at different free energies, i.e., $\Delta G_{r\,\mathrm{micropores}} \gg \Delta G_{r\,\mathrm{macropores}}$ (e.g., Swoboda-Colberg and Drever, 1993; Drever et al., 1994; van der Salm et al., 1996). The complexity of estimating field-based rates of dissolution as a function of ΔG_r is shown, for example, by a study of plagioclase weathering in granite by van der Weijden and Pacheco (2004).

The importance of the relation between the dissolution rate and ΔG_r is not limited to 'macroscopic' fluid-mineral interactions at near equilibrium conditions in natural environments. Much important information can also be deduced about the mechanism of hydrolysis, based on the mathematical form of the overall R–ΔG_r relation. Despite a significant number of recent experimental studies on feldspar dissolution rates as a function of ΔG_r, there is a surprising amount of disagreement with respect to both experimental results (i.e., mathematical form of R–ΔG_r data), as well as the respective models. Interpretations of R–ΔG_r data range from dissolution mechanisms based on complete ΔG_r-control of rates, ΔG_r-control coupled to Al inhibition of rates, and modification of rates and ΔG_r by precipitation of secondary phases.

2. Theoretical background

The Gibbs free energy ΔG_r that quantifies the deviation from equilibrium of an overall mineral dissolution reaction is defined as $\Delta G_r = \mathrm{R}T\ln(Q/K_{\mathrm{eq}})$, where Q is the ion activity product of the forward dissolution reaction and K_{eq} is the corresponding equilibrium constant (Q and K_{eq} must refer to exactly the same reaction). When written in a manner where the dissolving mineral is on the left side of the reaction, values of ΔG_r become increasingly negative as the thermodynamic 'distance' (i.e., solution undersaturation) from chemical equilibrium increases. By definition, $\Delta G_r = 0$ at chemical equilibrium, which is defined by the condition where the net forward (dissolution) reaction rate is equal to the net reverse (precipitation) reaction rate. The

term 'chemical affinity' is also frequently used in the literature, and is generally considered to be interchangeable with ΔG_r, i.e., $A = -\Delta G_r$.

While there are many possible forms that $f(\Delta G_r)$ can take, the following two conditions must be satisfied (e.g., Aagaard and Helgeson, 1982; Lasaga, 1995): $f(\Delta G_r) = 0$ at chemical equilibrium and $f(\Delta G_r) = 1$ as $\Delta G_r \to -\infty$ (i.e., dissolution conditions far from equilibrium, high solution undersaturation). The latter condition is related to the existence of a rate plateau, which must exist for all dissolution conditions, given that the overall rate $R = \vec{R} - \overleftarrow{R}$ (forward rate minus backward rate), and as $\Delta G_r \to -\infty$, $\vec{R} \gg \overleftarrow{R}$, so that $R = \vec{R}$. The exact mathematical form of $f(\Delta G_r)$ has been a source of continuous debate among geochemists for several decades. Even though a detailed discussion of the various forms of $f(\Delta G_r)$ is beyond the scope of this study, we very briefly describe the most widely used free energy formulation applied in geochemistry—the transition state theory-based $f(\Delta G_r)$. In its simplest form, the TST-$f(\Delta G_r)$ term can be written as (Lasaga, 1981; Aagaard and Helgeson, 1982)

$$f(\Delta G_r) = \left[1 - \exp\left(n\frac{\Delta G_r}{\mathrm{R}T}\right)\right]. \quad (3)$$

According to Lasaga et al. (1994) and Lasaga (1998), $n = 1$ for the breakdown of a single critical activated complex. When there is more than one elementary step (which reflects the complex nature of most dissolution reactions), and with all steps having reached steady state, then $n > 1$ in Eq. (3) above (Nagy et al., 1991). While Eq. (3) is often termed a derivation of TST, in reality the conceptual 'jump' from true TST to $f(\Delta G_r)$ given in Eq. 3 is based on collision theory and van't Hoff's rule (e.g., Aagaard and Helgeson, 1982).

Using the simplest TST-form of $f(\Delta G_r)$, one can thus express the overall rate of dissolution R for a mineral via the following equation (Aagaard and Helgeson, 1977, 1982; Lasaga, 1981, 1984; Murphy and Helgeson, 1987; and references therein)

$$R = k_+ \prod_i a_i^{n_i}(1 - \exp(\Delta G_r/\mathrm{R}T)) = k_+ \prod_i a_i^{n_i}(1 - Q/K_{\mathrm{eq}}). \quad (4)$$

The symbols and units are defined as in Eq. (2); note also that ΔG_r substitutes for $-A$, as originally given in Eq. (30) (Aagaard and Helgeson, 1982). In the above equation, the term $\prod_i a_i^{n_i}$ is more generalized than in Eqs. (1a) and (1b), such that a_i also includes all rate-determining species (H^+, OH^-, etc.). The importance of Eq. (4) cannot be overemphasized in that it provides a direct link between the kinetics of an overall reaction R and a thermodynamic quantity, ΔG_r. Since the development almost 30 years ago of overall rate laws using TST, new theoretical approaches have been developed that supersede the simple TST-based approach shown above (e.g., Nagy et al., 1991; Nagy and Lasaga, 1992; Burch et al., 1993; Oelkers et al., 1994; Oelkers, 2001; Lasaga and Lüttge, 2001, 2003, 2004a,b).

3. Materials and methods

3.1. Albite samples

The albite used in this study, from a pegmatite located near Amelia Court House, Virginia (USA), was purchased from Ward's Scientific Est. The composition of the albite used is given in Table 1 in Hellmann (1994). Sample preparation consisted of crushing, sieving, extracting visible mineral impurities, and repeated cleaning in an ethanol ultrasonic bath. The parent batch was coarse grained ($\phi = 1$–3 mm) and has a specific surface area (SSA) of $0.013\ \mathrm{m^2\ g^{-1}}$ (measured by multipoint BET using Kr, estimated accuracy is 20–30%; see Hellmann, 1994 for details). This material was used primarily in experiments run at far-from-equilibrium conditions. Smaller batches of finer grained material ($0.5 < \phi < 1$ μm; insufficient quantities for BET) were also prepared from the parent batch and used in experiments for intermediate to near equilibrium conditions. These batches had slightly higher specific surface areas (0.013–$0.052\ \mathrm{m^2\ g^{-1}}$) that were estimated by taking the original SSA ($0.013\ \mathrm{m^2\ g^{-1}}$) and multiplying by a geometric surface area factor (i.e., starting with a cubic grain of 2mm and subdividing it into smaller, equal-sized cubic grains; the factor used to increase SSA was based on the ratio of original to final geometric surface area). Our estimated specific surface areas of the finer grained batches are in very good accord with BET measurements of similar size fractions of alkali feldspars reported in Holdren and Speyer (1987) and for albite in Brantley et al. (1999) and Brantley and Mellott (2000).

The use of grains in this study, rather than finer powders, facilitated the circulation of fluid between the grains and thereby minimized chemical gradients with the bulk reactor fluid. Moreover, the surface coverage of grains covering the bottom of the reactor vessel was sparse enough to ensure monolayer coverage. In addition, coarse grains facilitate post-experimental surface studies using electron microscopy and spectroscopy techniques.

3.2. Experimental methods

3.2.1. Reactor systems

The experiments were conducted with two independent, continuously stirred hydrothermal flow-through systems (CSTR), a Parr 300 ml system and a Parr 50 ml system (for a detailed description, see Hellmann et al., 1997). To minimize corrosion, both systems incorporate Ti wetted parts (reactor, impellor, tubing). The 300 ml system uses an Isco syringe pump that enables ultra-precise and steady flow rates down to $0.001\ \mathrm{ml\ min^{-1}}$ (which corresponds to a 208.3-day residence time). The 50 ml system uses a Knauer HPLC pump that has a minimum flow rate capability of $0.01\ \mathrm{ml\ min^{-1}}$. All experiments were conducted at 150 °C at 1–2 MPa fluid pressure. At these P–T conditions, only a single liquid phase is present in the reactor. To mitigate against potential precipitation phenomena, the 300 ml system is equipped with a supplemental heating system that keeps the exit tubing (between reactor and back pressure regulator) at ~90 °C. The solution in the reactor was always well mixed due to the rotating impellor, but its speed was adjusted to avoid the entrainment of the grains into a suspended slurry.

3.2.2. Reactor input solution

The dissolution reactions were carried out at 150 °C and at basic pH. The choice of pH was specifically made to take advantage of the increased solubilities of Al oxy-hydroxides and silica gel in the basic pH region, thereby mitigating against their precipitation (note that precipitates ultimately complicate interpretation of the R–ΔG_r relation). All chemical reagents used were of high quality (analytical grade or better), including the pure deionized water ($\geqslant 17$ MΩ). To ensure long term pH stability, the input solutions were based on a boric acid pH buffer, using 0.05 M H_3BO_3 that was pH-adjusted to 10.0 (±0.05) at 25 °C using 1 N NaOH. The pH was measured with a Mettler pH electrode calibrated beforehand with commercial buffer solutions (pH 7.00, 10.00 at 25 °C). At the beginning of each experiment, the volume of the input solution filled the entire 20 or 50-

liter container (closed to atmosphere), thereby reducing CO_2 absorption and ensuring a high buffering capacity. During long-term experiments (>1 month), the pH of the input solution was measured periodically to verify that any decrease in pH did not exceed ~0.1 pH unit; any greater deviation was corrected for by the addition of a small amount of 1 N NaOH. The measured concentration of Na in each input solution ranged from ~0.039 to 0.043 m (900–1000 ppm).

A 'standard' input solution that is charge balanced at 25 °C, simulated using the EQ3NR code (Wolery, 1992), was based on the following input composition: 0.043 m Na, 0.05 m H_3BO_3, pH 10.0. Electrical balancing was achieved on H^+, yielding a pH of 9.96 at 25 °C (or 9.18 at 150 °C; pH not measured in situ). Electrical balancing on Na^+ resulted in Na concentrations higher than measured, and thus we chose to simulate all solutions with a charge balance on H^+ and constant 0.043 m [Na]. Nonetheless, whether the input solution was charge balanced on H^+ or Na^+, this had no significant effect on the calculated Gibbs free energies, even at dissolution close to equilibrium (difference in $\Delta G_r \leqslant 0.7$ kJ mol^{-1}). The calculated ionic strength of the input solution was 0.043 m; this remained constant even for exit solution compositions representative of dissolution conditions very close to equilibrium.

3.2.3. Experimental protocol and analytical procedures

The results reported here represent a series of experiments that were run over a period of 8 years. The experiments in this study differ from other studies in that we measured dissolution rates over a very extended range of Gibbs free energies (from −15.6 to −150 kJ mol^{-1}); in addition, we also conducted very long duration experiments at conditions close to equilibrium. The ΔG_r for each experiment was controlled in two ways: by the mass and specific surface area of solid in the reactor—increasing these lead to reaction at higher ΔG_r; by the fluid residence time, which was controlled by the flow rate—the lower the flow rate the higher the residence time, and thus the closer to equilibrium the dissolution reaction. The time period of each experimental run ranged from 4 to 5 days at far-from-equilibrium to 641 days at near equilibrium conditions. The chosen length of a particular run served to ensure the attainment of a hydrodynamic steady state (based on the injection of a minimum of 2–3 reactor volumes), and more importantly, a chemical steady state, as determined by relatively constant rates of release of Al and Si with time.

In the vast majority of cases, each individual experiment was run at a constant flow rate, but in a few cases, after the attainment of steady-state concentrations, the flow rate was changed to a new value(s) during the course of the experiment (referred to as multiple flow rate experiments). In all experiments, the input solutions were devoid of Al and Si. This is in contrast to most past studies where dissolution conditions close to equilibrium were achieved by using input solutions containing elevated concentrations of Al and Si (e.g., Burch et al., 1993; Oelkers et al., 1994; Gautier et al., 1994). Thus, in this study, with the exception of the relatively constant [Na] in the input solution, the ΔG_r associated with a particular rate was based on [Si] and [Al] that were produced solely by the dissolution process.

The exit solution from each experiment was collected periodically in order to determine the rates of dissolution as a function of time, and especially to ascertain whether constant concentrations (i.e., steady-state rates) were achieved. The chemistry of the solutions was in general measured immediately after sampling. The concentrations of Al and Si in the exit solution were measured by ICP (Perkin Elmer Optima 3300 DV) using matrix-matched standards and matrix blanks. An additional measure of [Si] was effected by (matrix-matched) silicomolybdate colorimetric analyses using an autoanalyzer (Technicon). The change in [Na] due to dissolution was negligible, and therefore [Na] was not systematically measured in the output. Measurements of the output pH showed decreases that depended on the flow rate, with changes up to 0.2 pH units (compared to input pH). However, at slow flow rates, sampling took ~7 days, and this probably resulted in an artificially low pH due to CO_2 adsorption in the small sample volume. According to EQ3NR calculations, the pH in the reactor decreased by at most 0.04 log units, this most likely representing a more accurate estimate of the maximum change in pH.

The analytical uncertainty in the measurements (i.e., a function of the precision and accuracy) was strongly dependent on the concentration range of Si and Al. The uncertainty estimates (1 SD) were based on repeated analyses of standard solutions and blanks. At concentrations $\geqslant$500 ppb the uncertainty in the Si and Al analyses was ~5%, and as the Si and Al concentrations decreased to 50 ppb, the uncertainty increased from ~5 to 15%. At concentrations $\leqslant$50 ppb, reported [Si] values were weighted heavily towards colorimetric analyses (analytical limit ~1 ppb). Decreases in [Si] from 50 → 10 → 3 ppb resulted in the following corresponding increases in the uncertainties: ~15 → 30 → 50%. With respect to [Al] in the range of 50 → 10 → 3 ppb (the ICP manufacturer's listed analytical limit for [Al] is 1.8 ppb, 3 σ), the corresponding uncertainties were estimated to increase as follows: ~15 → 50 → 100%. The ppm and ppb concentration units referred to above are defined as $mg_{element}/kg_{solution}$ and $\mu g_{element}/kg_{solution}$, respectively.

The mass loss rates have an intrinsically higher accuracy compared to concentration based rates, and this characteristic provided a useful and independent control of the dissolution rates, which was especially important for rates in the far-from-equilibrium free energy range. At intermediate to near equilibrium conditions, the agreement between the mass loss rates R_m and the aqueous dissolution rates R_{Si} and R_{Al} was generally very good. At far-from-equilibrium conditions (i.e., [Si], [Al] < 50 ppb), the divergence between the two types of rates tended to increase with decreasing ΔG_r, but in most cases, at least one of two aqueous rates (Si- or Al-based) had acceptable agreement ($\leqslant$20% difference) with the corresponding mass loss rate. In those few cases where experiments were run at multiple flow rates, mass-based rates could not be determined (and hence are not reported) for those flow rate regimes where both the initial and final masses could not be measured.

3.3. Experimental calculations

3.3.1. Dissolution rates

Albite dissolution rates for each experiment were determined using [Si] and [Al] measured as a function of time, as well as from change in sample mass measured at the end of each experiment (R_{Si}, R_{Al}, and R_m, respectively). The rates of dissolution (R_{Si}, R_{Al}) determined at the end of each run (or before a flow rate change during multiple flow rate experiments) represent steady-state rates, based on constant concentrations with respect to the time interval of the experiment. All rate calculations use a constant specific surface area measured before dissolution (see Section 3.1). Post-dissolution surface areas were not measured after each experiment due to: (1) insufficient sample mass for BET analysis (2) possible interference from porous altered surface layers (e.g., Casey et al., 1989) that are not representative of the surface area of the dissolving mineral surface.

The rate of albite dissolution based on [Si] and [Al] in the exit solution is determined from the following relation applicable to well-stirred flow-through reactors

$$R_{Si,Al} = \frac{C_{exit} \upsilon 10^{-6}}{M \delta m_t SSA}. \quad (5)$$

Here, R_{Si} or R_{Al} has units of mol m^{-2} s^{-1}, C_{exit} is the exit concentration of Si or Al (ppm), υ is the flow rate (ml s^{-1}), 10^{-6} is a conversion factor, M is the formula mass of Si or Al (g mol^{-1}), δ is a stoichiometric coefficient (albite: $\delta = 3$ for Si, $\delta = 1$ for Al), m_t is the estimated mass at time t (based on linear mass loss as a function of time) and SSA is the pre-dissolution specific surface area (m^2 g^{-1}). The calculated error in R_{Si} or R_{Al} is largely attributable to the terms SSA and C_{exit}. Using standard error propagation methods, representative errors in R_{Si} or R_{Al} over a wide range of ΔG_r have been calculated and are discussed further on.

The rate of dissolution based on mass loss R_m (mol m^{-2} s^{-1}) is given by

$$R_m = \frac{m_i - m_t}{MW \Delta t \frac{(m_i + m_t)}{2} SSA}, \quad (6)$$

where m_i and m_t are the original mass and mass at time t (g), MW is the molecular weight of albite (262.219 g mol^{-1}), Δt is time elapsed (s), and SSA is the specific surface area (m^2 g^{-1}). The error in the final value of R_m (at end of an experiment) is due almost exclusively to uncertainty in the SSA term, and is estimated to be 20–30%. Note that R_m represents an average rate over time interval Δt, and not an instantaneous rate, as is the case with element-based rates (Eq. (5)).

When R_{Si}, R_{Al}, and/or R_m had significant scatter (far-from-equilibrium rates, e.g., Fig. 1A), the reported values for the final rates were based on rate averages derived from the last two data points, and not just the final data point. In Table 1, such experiments are recognizable by the use of two numbers following the experiment ID; e.g., 50 F-7-8.

3.4. Theoretical calculations

3.4.1. Free energy of dissolution ΔG_r

The free energy of dissolution, defined as $\Delta G_r = RT \ln (Q/K_{eq})$, was calculated using the code EQ3NR (Wolery, 1992). When running the code, we used the LLNL 'composite' (com) data base (see Wolery, 1992). Input parameters for each EQ3NR calculation were as follows: [Na] = 0.043 m (1000 ppm); [H_3BO_3] = 0.05 m; pH (150 °C) = 9.18; this last parameter, however, was allowed to vary since the code charge balanced the solution using [H^+]. The values of ΔG_r calculated by EQ3NR correspond to the following dissolution reaction

$$NaAlSi_3O_8 + 4H^+ \leftrightarrow 2H_2O + Al^{3+} + Na^+ + 3SiO_2(aq) \quad (7)$$

The EQ3NR thermodynamic data base fixes log $K_{eq} = -1.20$ at 150 °C for the reaction given in Eq. (7). The reaction shown below (log $K_{eq} = 13.21$ at 150 °C, EQ3NR)

$$Al(OH)_4^- + 4H^+ \leftrightarrow 4H_2O + Al^{3+} \quad (8)$$

can be summed with the dissolution reaction in Eq. (2) (log $K = -14.42$ at 150 °C) to yield the (EQ3NR) dissolution reaction given in Eq. (7). We note that for internal consistency, we used log $K_{eq} = 13.21$, even though alternative values for Eq. (8) exist in the literature (log $K_{eq} = 13.55$, Bénézeth et al., 2001; log $K_{eq} = 13.73$, Tagirov and Schott, 2001). Aluminum–Si complexes (specifically, $Al(OH)_3H_3SiO_4^-$) were not significant at experimental conditions, based on tabulated equilibrium constants in Tagirov and Schott (2001).

Evaluation of the dissolution reaction given by Eq. (7) is based on pure albite with unit activity. Activity coefficients for aqueous species were calculated using the B-dot equation. The ion activity product Q for Eq. (7) depends on the measured values of [Si] and [Al] in the reactor output solution ([Na] is constant). Representative uncertainties in ΔG_r, which are a function of the uncertainties in Q, were calculated using EQ3NR for two

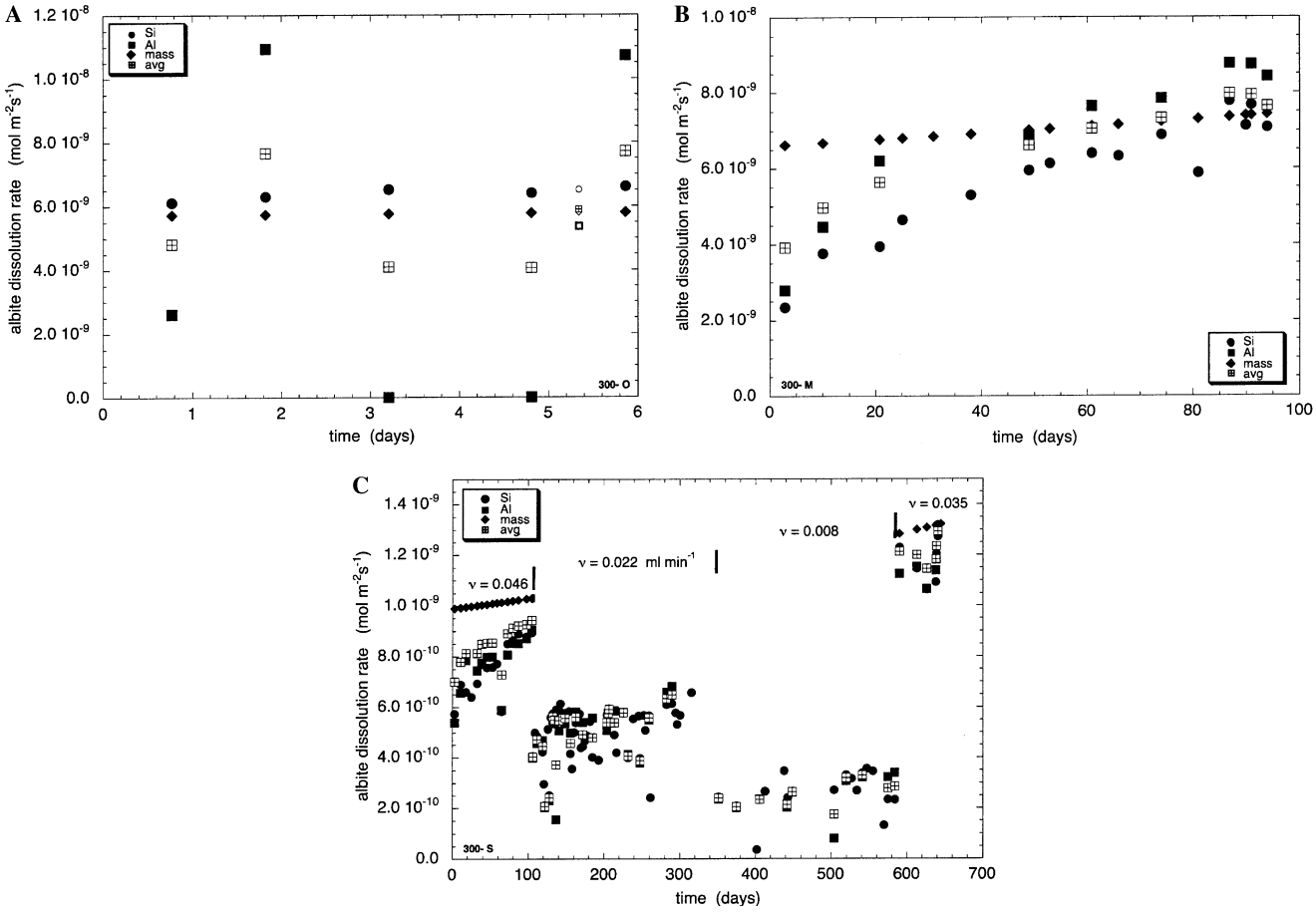

Fig. 1. Dissolution rates of albite as a function of time and ΔG_r. R_{Si} and R_{Al} are based on raw [Si] and [Al], R_m is based on a linear mass loss with time, and $\overline{R}$ is the unweighted average of R_{Si}, R_{Al}, and R_m. (A) Rate evolution at far-from-equilibrium conditions, $\Delta G_r = -131$ kJ mol^{-1} at end of experiment. Note the rapid achievement of steady-state behavior of R_{Si}. The scatter in R_{Al} is due to analytical uncertainty. Open symbols ($t \approx 5.3$ days) represent average rates based on the last two data points. (B) Rate evolution at conditions closer to equilibrium; $\Delta G_r = -43$ kJ mol^{-1} at end of experiment. Note the significantly longer times necessary for the achievement of steady-state R_{Si} and R_{Al}, which is also marked by convergence of R_{Si}, R_{Al}, and R_m. (C) Rate evolution at near equilibrium conditions. This experiment was run using variable flow rates (v) over extended periods of time, in order to change concomitantly ΔG_r and the dissolution rate. The respective (terminal) values of ΔG_r for the four flow regimes ranged from −25 to −21 kJ mol^{-1}. The monotonic increase of R_m with time is an artifact—see Appendix A for details.

Table 1
Summary of experimental and calculated data concerning the dissolution of albite

Expt.[a]	Time[b] (days)	Mass i[c] (g)	Mass t[d] (g)	Δmass[e] (g)	Surf area[f] ($m^2\ g^{-1}$)	Flow rate ($ml\ min^{-1}$)	[Si] (m)	[Al] (m)	[Si]/[Al]	R_{Si}[g] ($mol\ m^{-2}\ s^{-1}$)	R_{Al}[h] ($mol\ m^{-2}\ s^{-1}$)	R_{mass}[i] ($mol\ m^{-2}\ s^{-1}$)	R_{avg}[j] ($mol\ m^{-2}\ s^{-1}$)	log R_{avg} ($mol\ m^{-2}\ s^{-1}$)	ΔG_r ($kJ\ mol^{-1}$)	log [Al] (m)	log [Si] (m)
50 B-5	11.67	0.57952	0.54100	0.07821	0.0220	0.540	3.970e−05	1.379e−05	2.88	1.001e−08	1.043e−08	1.182e−08	1.075e−08	−7.969	−59.79	−4.861	−4.401
50 C-17	9.78	0.34916	0.31342	0.03648	0.0325	0.550	4.059e−05	1.286e−05	3.16	1.218e−08	1.157e−08	1.499e−08	1.291e−08	−7.889	−59.81	−4.891	−4.392
50 D-28	17.76	0.12474	0.10240	0.02234	0.0390	1.650	7.976e−06	2.224e−06	3.59	1.831e−08	1.531e−08	1.254e−08	1.539e−08	−7.813	−83.18	−5.653	−5.098
50 E-18	10.19	0.06021	0.04522	0.01499	0.0520	3.160	2.528e−06	7.598e−07	3.33	1.887e−08	1.702e−08	2.369e−08[x]	1.534e−08	−7.814	−99.09	−6.119	−5.597
50 F-7-8	7.61	0.03541	0.03396	0.00171	0.0300	2.430	1.602e−06	3.150e−07	5.09	1.910e−08	1.192e−08	8.107e−09	1.304e−08	−7.885	−107.00	−6.502	−5.795
50 G-9	18.08	0.03700	0.02940	0.00760	0.0300	1.980	2.101e−06	3.706e−07	5.67	2.620e−08	1.387e−08	1.863e−08[x]	2.003e−08	−7.698	−103.57	−6.431	−5.678
50 H-8-9	11.57	0.00848	0.00778	0.00073	0.0360	2.800	1.200e−06[x]	7.413e−08	16.2[x]	6.660e−08[x]	1.234e−08	9.061e−09	1.070e−08	−7.971	−115.14	−7.130	−5.921[x]
50 I-2-3	4.39	0.01260	0.01225	0.00040	0.0290	5.200	8.902e−08	1.482e−07[x]	0.60[x]	7.261e−09	3.645e−08[x]	9.718e−09	8.489e−09	−8.071	−140.16	−6.829[x]	−7.051
50 J-13	67.98	0.37735	0.23502	0.14423	0.0290	0.330	5.483e−05	1.612e−05	3.40	1.475e−08	1.301e−08	1.041e−08	9.797e−09[*]	−8.009	−55.83	−4.793	−4.261
50 K-16	77.09	0.54836	0.38811	0.16025	0.0290	0.099	1.716e−04	5.685e−05	3.02	8.387e−09	8.335e−09	6.757e−09	6.496e−09[*]	−8.187	−39.27	−4.245	−3.765
50 L-20	115.87	5.78929	4.95088	0.83841	0.0300	0.104	4.888e−04	1.835e−04	2.66	1.902e−09	2.141e−09	1.983e−09	2.008e−09	−8.697	−23.86	−3.736	−3.311
50 L-35	156.89	5.78929	†	†	0.0300	0.039	6.815e−04	2.405e−04	2.83	1.068e−09	1.131e−09	†	1.100e−09	−8.959	−19.27	−3.619	−3.167
50 M-25	255.99	7.09517	4.92103	2.25167	0.0260	0.104	5.264e−04	1.811e−04	2.91	2.375e−09	2.451e−09	2.400e−09	2.026e−09[*]	−8.693	−23.11	−3.742	−3.279
50 N-15	114.91	14.01126	13.05675	0.95451	0.0390	0.061	8.537e−04	3.385e−04	2.52	5.694e−10	6.772e−10	6.946e−10	6.471e−10	−9.189	−15.55	−3.470	−3.069
50 N-25	188.80	14.01126	†	†	0.0390	0.006	8.456e−04	2.820e−04	3.00	6.177e−11	6.180e−11	†	6.178e−11	−10.21	−16.33	−3.550	−3.073
50 N-31	227.00	14.01126	12.12569	1.90045	0.0390	0.062	7.732e−04	2.862e−04	2.70	5.600e−10	6.219e−10	7.194e−10	6.337e−10	−9.198	−17.25	−3.543	−3.112
300 A-14	16.85	1.34999	1.31022	0.03977	0.0195	0.084	2.197e−04	7.498e−05	2.93	4.013e−09	4.108e−09	4.016e−09	4.046e−09	−8.393	−35.65	−4.125	−3.658
300 A-25	26.69	1.34999	†	†	0.0195	0.040	3.297e−04	1.197e−04	2.75	2.919e−09	3.180e−09	†	3.050e−09	−8.516	−29.64	−3.922	−3.482
300 A-34	35.67	1.34999	1.26582	0.08417	0.0195	0.091	2.136e−04	7.349e−05	2.91	4.376e−09	4.516e−09	4.084e−09	4.325e−09	−8.364	−36.02	−4.134	−3.670
300 B-7-8	8.89	0.11856	0.11662	0.00202	0.0130	14.94	5.341e−07	3.150e−07[x]	1.70[x]	2.905e−08	5.170e−08[x]	6.291e−09	1.767e−08	−7.753	−118.60	−6.502[x]	−6.272
300 C-3-4	2.73	0.13167	0.13093	0.00089	0.0156	12.80	1.246e−06[x]	2.780e−07[x]	4.48[x]	4.352e−08[x]	2.762e−08[x]	5.857e−09	5.857e−09	−8.232	−110.34	−6.556[x]	−5.904[x]
300 D-4-5	3.32	0.12037	0.11956	0.00089	0.0156	11.15	1.424e−07	1.853e−07	0.77	4.673e−09	1.827e−08	5.774e−09	9.572e−09	−8.019	−134.42	−6.732	−6.846
300 E-3-4	3.31	0.17078	0.16923	0.00179	0.0169	9.070	3.561e−07	2.409e−07	1.48	6.275e−09	1.274e−08	7.187e−09	8.734e−09	−8.059	−123.82	−6.618	−6.448
300 F-3-4	3.39	0.12887	0.12781	0.00201	0.0182	7.000	3.205e−07	3.521e−07	0.91	5.366e−09	1.768e−08	5.920e−09	9.655e−09	−8.015	−123.60	−6.453	−6.494
300 G-5	6.89	0.13584	0.13378	0.00206	0.0195	4.980	4.985e−07	3.706e−07	1.34	5.287e−09	1.179e−08	5.026e−09	7.368e−09	−8.133	−118.75	−6.431	−6.302
300 H-4	5.01	0.16118	0.15888	0.00230	0.0195	2.980	8.189e−07	6.301e−07	1.30	4.376e−09	1.010e−08	6.493e−09	6.990e−09	−8.156	−111.65	−6.201	−6.087
300 I-7	15.87	0.16131	0.15015	0.01262	0.0228	1.000	5.377e−06	1.631e−06	3.30	8.725e−09	7.939e−09	8.739e−09	8.468e−09	−8.072	−88.43	−5.788	−5.270
300 J-6	11.89	0.20378	0.19411	0.00967	0.0195	2.010	1.994e−06	1.038e−06	1.92	5.882e−09	9.184e−09	9.254e−09	8.107e−09	−8.091	−100.50	−5.984	−5.700
300 K-15	32.00	0.39309	0.36006	0.03303	0.0156	0.490	1.506e−05	6.263e−06	2.40	7.299e−09	9.107e−09	7.755e−09	8.054e−09	−8.094	−72.82	−5.203	−4.822
300 L-23	92.94	0.51019	0.34785	0.16234	0.0169	0.350	4.273e−05	1.631e−05	2.62	1.413e−08	1.618e−08	1.063e−08	1.114e−08[*]	−7.953	−58.43	−4.788	−4.369
300 M-16	93.96	0.73128	0.56700	0.16428	0.0160	0.089	1.300e−04	5.152e−05	2.52	7.083e−09	8.423e−09	7.430e−09	6.713e−09[*]	−8.173	−42.57	−4.288	−3.886
300 N-14	23.98	0.04033	0.02554	0.01479	0.0330	1.000	1.460e−06	5.930e−07	2.46	9.623e−09	1.173e−08	2.505e−08[x]	8.390e−09[*]	−8.076	−105.76	−6.227	−5.836
300 O-4-5	5.34	0.00651	0.00635	0.00018	0.0364	1.000	2.706e−07	7.413e−08	3.65	6.508e−09	5.362e−09	5.790e−09	5.887e−09	−8.230	−130.86	−7.130	−6.568
300 P-10-11	7.93	0.01108	0.01086	0.00030	0.0300	2.980	1.602e−07	5.559e−08	2.88	8.141e−09	8.474e−09	3.678e−09[x]	8.308e−09	−8.081	−137.41	−7.255	−6.795
300 Q-2-3	4.54	0.01240	0.01176	0.00073	0.0290	7.040	7.477e−08	1.853e−08	4.04	8.555e−09	6.333e−09	1.771e−08[x]	7.444e−09	−8.128	−149.32	−7.732	−7.126
300 R-22	129.04	0.27526	0.17854	0.09672	0.0230	0.068	1.022e−04	3.421e−05	2.99	9.401e−09	9.441e−09	6.339e−09	6.648e−09[*]	−8.177	−46.58	−4.466	−3.991
300 S-15	104.71	4.53525	4.16344	0.37181	0.0350	0.046	5.099e−04	1.720e−04	2.96	8.942e−10	9.048e−10	1.030e−09	9.429e−10	−9.026	−23.64	−3.765	−3.293
300 S-61	289.67	4.53525	†	†	0.0350	0.022	6.057e−04	2.245e−04	2.70	6.141e−10	6.828e−10	†	5.694e−10[*]	−9.245	−20.81	−3.649	−3.218
300 S-85	574.90	4.53525	†	†	0.0350	0.008	4.907e−04	2.249e−04	2.18	2.342e−10	3.221e−10	†	1.992e−10[*]	−9.701	−23.07	−3.648	−3.309
300 S-92	640.92	4.53525	2.25938	2.29023	0.0350	0.038	4.777e−04	1.612e−04	2.96	1.272e−09	1.287e−09	1.318e−09	8.595e−10[*]	−9.066	−24.58	−3.793	−3.321

[a] Last aqueous sample collected before termination (or change in flow rate) of run; expts. with 2-number suffix refer to average of last two samples—applies to concentrations, times, rates, and ΔG_r—see text for details. [b] Sampling time from start of Expt. [c] Initial mass, start of Expt. (also for multiple flow rate expts.). [d] Measured mass time t (t = end Expt., or estimated mass during run); † mass (t) not measurable. [e] Mass i − mass t (note that final mass corresponds to time when sample recovered, and not last aqueous sampling); † mass difference not measurable. [f] Pre−dissolution BET specific surface area. [g,h,i] Raw albite dissolution rate based on [Si], [Al], mass loss- Figs. 2A–C; † R_m not measurable. [j] Avg. dissolution rate, plotted in Figs. 3, based on (g + h + i/3), excluding rates (marked by [x]) exceeding ± 1 SD in respective rate plateau regions of Figs. 2A–C; [x] values not used for calculation of Si/Al, R_{avg}, log R_{avg}, log [Al], log [Si]; [*] avg. dissolution rate adjusted (decreased), based on correction factor for increasing SSA (see Appendix A).

representative experiments: one at far from equilibrium using [Si] ±30% and [Al] ±50%; the second at near equilibrium using [Si] ±5% and [Al] ±5%. The highest calculated uncertainty in ΔG_r was 5.2%, and corresponded to the far-from-equilibrium case, $\Delta G_r = -118$ kJ mol^{-1}. The uncertainty in ΔG_r due to K_{eq} was not calculated since the error is not known (error probably in range of a few kJ mol^{-1}). Nonetheless, using a different value for K_{eq} will only shift the origin, but not change the R–ΔG_r relation (Burch et al., 1993).

4. Results and discussion

4.1. Behavior of dissolution rate curves as a function of ΔG_r

Figs. 1A–C show typical R_{Si}, R_{Al}, and R_m data as a function of time and ΔG_r, with ΔG_r representative of far-from-equilibrium, transition equilibrium, and near equilibrium conditions. The time evolution of a typical experiment at far-from-equilibrium conditions (−131 kJ mol^{-1}) is shown in Fig. 1A. The R_{Si} curve shows steady-state behavior and excellent agreement with R_m over the entire experimental duration (6 days). The scatter in R_{Al} is due to analytical uncertainty associated with very low [Al] at these far-from-equilibrium conditions. Based on 20 experiments run at far-from-equilibrium conditions ($-150 \leqslant \Delta G_r \leqslant -70$ kJ mol^{-1}), the rapid increase to steady-state rates occurs very rapidly, almost in a step function-like manner, over periods rarely exceeding 1 day (in many cases $t < 1$ day). This rapid approach to equilibrium is in accord with similar results determined by Hellmann, 1995 (see Fig. 5 therein), where steady-state rates at temperatures ⩾ 100 °C and basic pH were achieved in just several hours.

The dissolution rates in the transition equilibrium regime ($-70 \leqslant \Delta G_r \leqslant -25$ kJ mol^{-1}) increase to comparatively lower steady-state rates over longer periods of time, requiring a minimum of at least 5–10 days, and often significantly more, as evidenced in Fig. 1B. For this particular experiment ($\Delta G_r = -43$ kJ mol^{-1} at the termination of the run) R_{Si} and R_{Al} show a rapid monotonic increase over approximately the first 50–60 days before becoming roughly stable and converging to the same approximate value; note convergence with R_m, as well. The apparent slight increase in R_{Si} and R_{Al} at $t > 60$ days is most likely not real (see Appendix A). The overall behavior of the R_m curve is explained in Appendix A.

Experiments run even closer to equilibrium ($\Delta G_r > -25$ kJ mol^{-1}) required up to 100 days for the initial stabilization of rates. Experiments at these conditions were either conducted at a single flow rate, or in a few cases, with multiple flow rates over extended periods of time, as shown in Fig. 1C. For the case illustrated, the initial flow rate regime was followed by two successive decreases in the flow rate, in order to change concomitantly ΔG_r and the dissolution rates R_{Si} and R_{Al}. Towards the end of this experiment, the flow rate was increased again, resulting in another change in R_{Si} and R_{Al}. In each case, the flow rate changes induced new rates of dissolution that stabilized rapidly (i.e., $t < 100$ days). The agreement between steady-state R_{Si} and R_{Al} is very good at each flow rate, with the exception of some outlier rates. Values for R_m could not be determined for the intermediate flow rate regimes, and thus are not shown. The respective values of ΔG_r for the four flow regimes range from −25 to −21 kJ mol^{-1}. Certain aspects of the time evolution of R_{Si}, R_{Al}, and R_m are discussed in detail in Appendix A.

In summary, the time necessary for the achievement of steady-state dissolution rates, based on dissolution starting in totally unsaturated solutions, increases with increasing ΔG_r, even though steady-state rates of dissolution decrease with increasing ΔG_r. This observation is not surprising since the 'thermodynamic distance' (i.e., $\Delta G_{r\,\text{initial}} \approx -\infty \rightarrow \Delta G_{r\,\text{steady state}}$) traversed by a mineral-fluid system increases with increasing free energy ($\Delta G_r \rightarrow 0$). On the other hand, all dissolution rates (experiments starting from unsaturated solutions) increase from $R = 0$ (at $t = 0$) to steady-state rates (Figs. 1A–C), irrespective of the final ΔG_r attained. This is a surprising result, given that the achievement of steady-state rates near equilibrium ($\Delta G_r > -25$ kJ mol^{-1}) requires the mineral-solution system to traverse initial, far-from-equilibrium ΔG_r conditions that correspond to faster dissolution rates, and hence one might expect rates to first increase (from zero) and then decrease to final steady-state rates. However, this observation would have to be confirmed with closer-spaced sampling during the first 24 h of dissolution.

We also address one final item- the temporal evolution of steady-state rates with ΔG_r is not related to the hydrodynamics of the continuously stirred reactors we used. In other words, the time scales necessary for hydrodynamic steady states to be established for a particular flow rate (based on criterion of 2–3 reactor volumes) were inferior to those required for achievement of chemical steady states based on constant dissolution rates.

4.2. Steady-state dissolution rates as a function of ΔG_r

Figs. 2A–C illustrate the steady-state rates of dissolution as a function of ΔG_r. The three sets of rates shown, R_{Si}, R_{Al}, and R_m, are based on the respective original concentrations and mass differences measured at the termination of each experiment (or concentrations measured before a flow rate change during multiple flow rate experiments), and have not been modified by any data treatment schemes. To the best of our knowledge, this overall data set represents mineral dissolution rates measured over the largest continuous range of ΔG_r to date. Table 1 provides the measured steady-state concentrations of Si and Al, changes in sample mass, steady-state albite dissolution rates R_{Si}, R_{Al}, R_m, overall average rates of dissolution $\overline{R}$, and corresponding values of ΔG_r for all experiments.

Referring to Figs. 2A–C, all three R–ΔG_r data sets show overall behavior that is highly non-linear and sigmoidal. The scatter and presence of outliers in R_{Si}, and especially R_{Al}, at $\Delta G_r < -70$ kJ mol^{-1} are primarily due to analytical uncertainties in [Si] and [Al] at very low concentrations; the

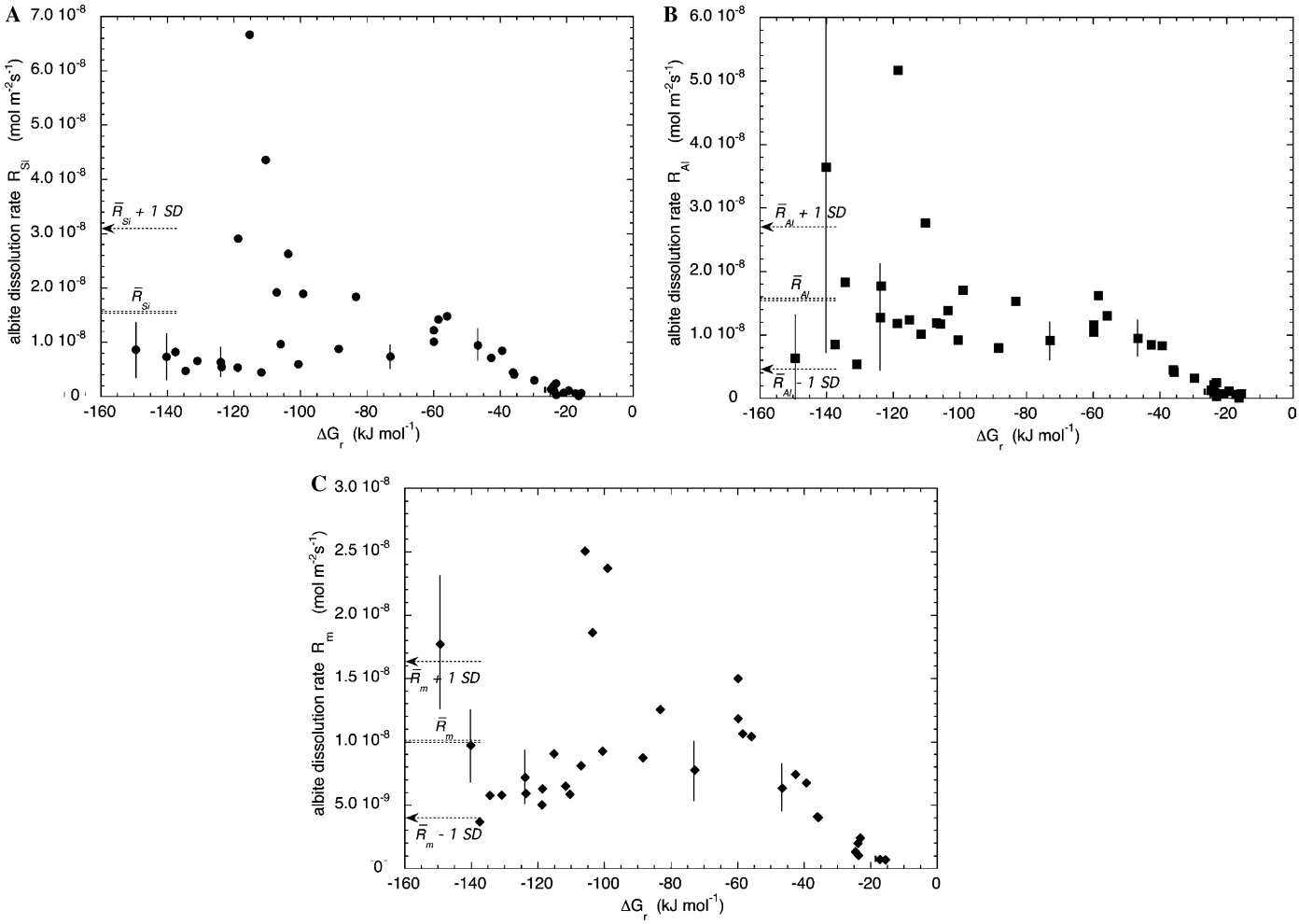

Fig. 2. Measured rates of albite dissolution R_{Si}, R_{Al}, R_m as a function of the free energy of dissolution ΔG_r, based on the entire data set using original (uncorrected) terminal values of, respectively, [Si] (A), [Al] (B), and change in mass (C). The scatter and presence of outliers in R_{Si} and particularly R_{Al}, in the range $\Delta G_r < -70$ kJ mol^{-1}, are primarily due to analytical uncertainties in [Si] and [Al]. Within the rate plateau region ($\Delta G_r < -70$ kJ mol^{-1}), the mean and standard deviation (± 1 SD, dashed lines) are shown for R_{Si}, R_{Al}, and R_m. Outliers (exceeding ± 1 SD in range $\Delta G_r < -70$ kJ mol^{-1}) were subsequently excluded with respect to the calculation of the mean (unweighted) rate $\overline{R}$ for each experiment—see Fig. 3A. The error bars represent estimated uncertainties (1 SD) in representative individual rates over the entire range of ΔG_r.

exact reason for the outliers in R_m is not known, but they most probably are an experimental artifact. The R_m–ΔG_r data differ slightly from R_{Si}–ΔG_r and R_{Al}–ΔG_r in that the former data form a pronounced 'hump' or maximum in the ΔG_r range of ~ -50 to -85 kJ mol^{-1}; it is not certain whether this feature is statistically valid, however. Representative uncertainties (± 1 SD) for the individual rates R_{Si}, R_{Al}, R_m are also shown in Figs. 2A–C, and are based on propagation of relative errors in the rate calculations. In general, the magnitudes of the error bars decrease significantly with increasing ΔG_r, due to decreasing analytical uncertainty in [Si] and [Al]. Note also that within a given range of ΔG_r the size of each error bar depends quite strongly on the absolute rate (i.e., concentration) measured (e.g., see Fig. 2B, $\Delta G_r < -70$ kJ mol^{-1}, ± 1 SD R_{Al}).

Despite the scatter of the individual R_{Si}, R_{Al}, and R_m in the region $\Delta G_r < -70$ kJ mol^{-1}, the data taken together suggest that the rates are constant and independent of ΔG_r; this is often referred to as a rate 'plateau' (Nagy and Lasaga, 1992). As far as we know, this is the first unequivocal experimental evidence for the existence of an extended rate plateau over a large range of ΔG_r. It is important to note that in this plateau region the rates are also independent of aqueous [Al] and [Si]. Many past studies have extrapolated the existence of extended dissolution rate plateaus, but without the necessary supporting data (e.g., Burch et al., 1993). An exception to this are the rate plateaus associated with Al-rich input solutions (e.g., Oelkers et al., 1994; Gautier et al., 1994).

The mean plateau rates and associated ± 1 SD calculated from each set of uncorrected rates R_{Si}, R_{Al}, and R_m over the free energy range $\Delta G_r < -70$ kJ mol^{-1} are as follows: $\overline{R}_{Si} = (1.54 \pm 1.58) \times 10^{-8}$, $\overline{R}_{Al} = (1.57 \pm 1.12) \times 10^{-8}$, and $\overline{R}_m = (1.01 \pm 0.62) \times 10^{-8}$ mol m^{-2} s^{-1} (shown in Figs. 2A–C). Individual outlier rates exceeding the respective limits of $\overline{R}_{Si} \pm 1SD_{Si}$, $\overline{R}_{Al} \pm 1SD_{Al}$, and $\overline{R}_m \pm 1SD_m$ were subsequently excluded for the calculation of the overall

mean (un-weighted) rate $\overline{R}$ for each experiment in the range $\Delta G_r < -70$ kJ mol^{-1}. The mean plateau rates listed above compare favorably with far-from-equilibrium rates that can be derived from the literature. Using a compilation of albite dissolution rates derived at basic pH and $T = 8$–300 °C (Table 3 and Fig. 10, Blum and Stillings, 1995; note we excluded the data of Oelkers et al. (1994) which diverge significantly from the regressed data), we regressed log k_+ vs. $1/T(1000)$ to obtain an activation energy of $E_a = 60$ kJ mol^{-1} K^{-1}. Using the relation $R = k_+(a_{OH^-})^n$, the Arrhenius equation, and $E_a = 60$ kJ mol^{-1} K^{-1} to determine k_+ at 150 °C, two dissolution rates (at pH 9.18 and $T = 150$ °C) were derived: 7.3×10^{-9} and 2.3×10^{-8} mol m^{-2} s^{-1}, depending on whether $n = 0.5$ or $n = 0.3$, respectively (values for n are limiting values retrieved from Table 3, Blum and Stillings, 1995). The important point is that these two rates estimated from the literature bracket the mean plateau rates $\overline{R}_{Si}$, $\overline{R}_{Al}$, and $\overline{R}_m$ determined in this study. In addition, this agreement in rates also demonstrates that the boric acid buffer solution did not have any significant effect on the measured rates.

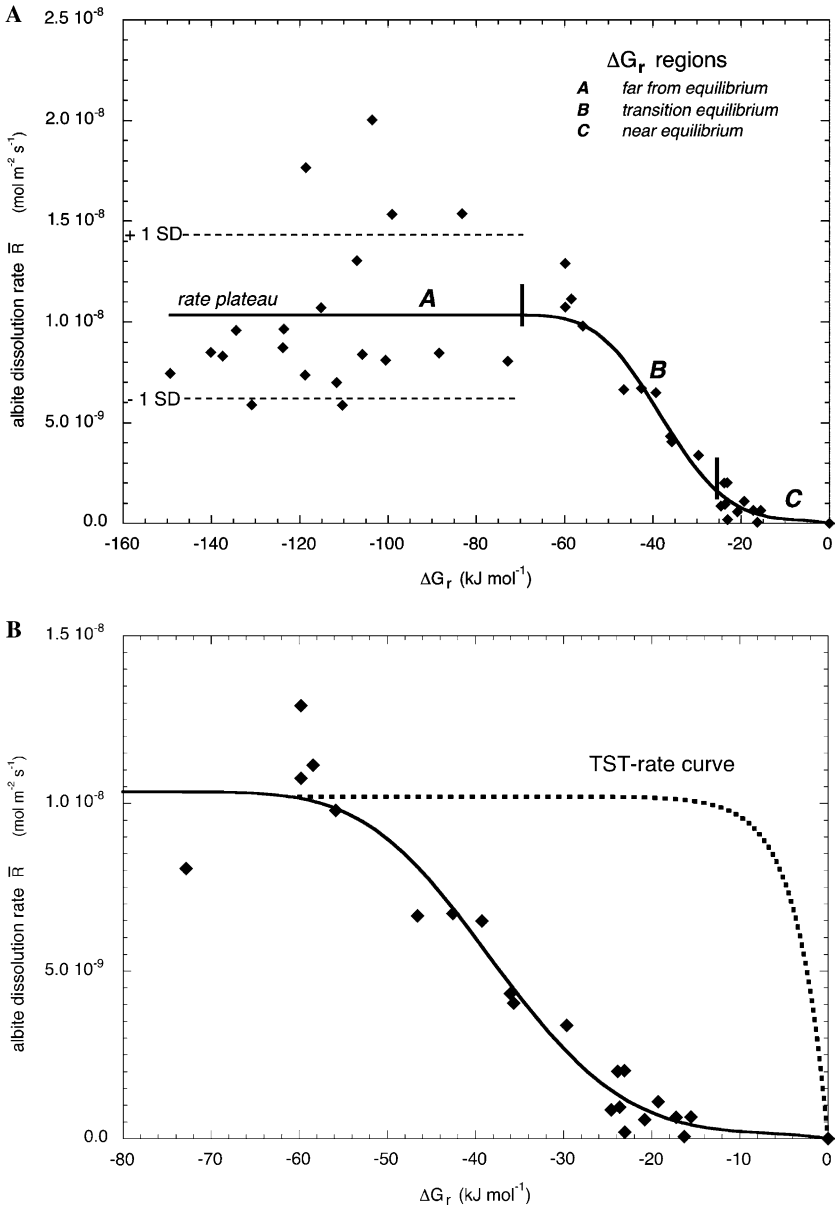

Fig. 3. (A) Average rates of albite dissolution for each experiment ($\overline{R} = (R_{Si} + R_{Al} + R_m)/3$) as a function of ΔG_r, compared to smooth curve fit based on an overall rate expression (Eq. (9)) composed of two parallel rate laws. The R–ΔG_r data and the curve fit are highly non-linear and show a sigmoidal trend, and are characterized by three distinct regions, whose exact limits are somewhat subjective: $\Delta G_r < -70$ kJ mol^{-1} represents 'far-from-equilibrium' dissolution and a rate plateau (bracketed by ±1 SD), here the rates are constant and independent of ΔG_r, [Si], and [Al]; the 'transition equilibrium' region, $-70 \leqslant \Delta G_r \leqslant -25$ kJ mol^{-1}, characterized by rates with a strong inverse dependence on ΔG_r; the 'near equilibrium' region, $-25 < \Delta G_r \leqslant 0$ kJ mol^{-1}, where the rates show a much less pronounced inverse dependence on ΔG_r. Note that the hypothetical datum $R = 0$, $\Delta G_r = 0$ represents chemical equilibrium. (B) Comparison of fitted rate curve with TST-rate curve based on Eq. (4).

4.3. Overall R–ΔG_r relation

Fig. 3 shows the average rates $\overline{R}$ as a function of the free energy, based on the relation $\overline{R} = (R_{Si} + R_{Al} + R_m)/3$ for each experiment (except certain multiple flow experiments where R_m could not be determined). In a few cases values of $\overline{R}$ were adjusted (decreased) to correct for changing specific surface area, but this had no influence on the general behavior of the $\overline{R}$–ΔG_r relation, as detailed in Appendix A. The sigmoidal relation between $\overline{R}$ and ΔG_r is characterized by three distinct regions, whose exact limits are somewhat subjective. The region defined by $\Delta G_r < -70$ kJ mol^{-1} represents far-from-equilibrium dissolution and a rate plateau, with a mean dissolution rate $\overline{R} = 1.02 \times 10^{-8}$ mol m^{-2} s^{-1}. In the plateau region the dissolution rates are constant and independent of ΔG_r and aqueous [Si] and [Al]. The second region, which we call the 'transition equilibrium' region ($-70 \leqslant \Delta G_r \leqslant -25$ kJ mol^{-1}), is characterized by a sharp decrease in dissolution rates with increasing ΔG_r, indicating a very strong inverse dependence of the rates on free energy. Dissolution closest to equilibrium, defined by $\Delta G_r > -25$ kJ mol^{-1}, represents the 'near equilibrium' region where the rates decrease with increasing free energy as chemical equilibrium is approached. In this region, the dependence of the rates on the free energy is much weaker than in the transition equilibrium region. Note that Fig. 3A also includes a 'theoretical' data point, $\Delta G_r = 0$, $\overline{R} = 0$, that represents chemical equilibrium.

The data shown in Fig. 3A are represented by a smooth curve fit based on an overall rate law (adapted from Burch et al., 1993) that represents the sum of two parallel reactions

$$R = k_1[1 - \exp(-ng^{m_1})] + k_2[1 - \exp(-g)]^{m_2}, \quad (9)$$

where k_1 and k_2 are rate constants that have been determined by regression, yielding, respectively, the values 1.02×10^{-8} and 1.80×10^{-10} mol m^{-2} s^{-1}, $g \equiv |\Delta G_r|/\mathrm{R}T$ is a dimensionless number, and n, m_1, and m_2 are adjustable fitted parameters ($n = 7.98 \times 10^{-5}$, $m_1 = 3.81$ and $m_2 = 1.17$). The rate expression on the right side (Eq. (9)) represents the rate in the near equilibrium region, which is compatible with TST (given that $m_2 \approx 1$; see Eq. (3)). The rate expression on the left side (Eq. (9)) expresses both the sharp change in rates in the transition equilibrium region, as well as the rate plateau (note that $k_1 = 1.02 \times 10^{-8}$ mol m^{-2} s^{-1} equals the plateau rate).

The rate expression given in Eq. (9) does not represent a unique fit to the experimental data. An equivalent fit, with the same correlation coefficient ($R = 0.83$), is represented by the following expression based on a single rate law

$$R = k_1[1 - \exp(-ng^{m_1})]. \quad (10)$$

This curve fit equation is identical to the left hand rate law term in Eq. (9), except that for this case $k_1 = 1.03 \times 10^{-8}$ mol m^{-2} s^{-1}, $n = 9.75 \times 10^{-5}$, and $m_1 = 3.74$. The implications of using a rate equation as in Eq. (9) are beyond the scope of this article, and will be discussed in a future study.

The overall R–ΔG_r relation, illustrated by the smooth curve fit in Fig. 3B, is sigmoidal and highly non-linear. In comparison, the R–ΔG_r relation based on a simple TST rate expression, such as given by Eq. (4), displays a completely different mathematical form, as shown in Fig. 3B. The disparity between the two rate curves over the interval $\Delta G_r > -50$ kJ mol^{-1} is evidence that a simple TST rate expression does not accurately predict albite dissolution rates as a function of ΔG_r (see similar comparisons in Burch et al., 1993 and Oelkers et al., 1994). In practical terms, the use of the TST rate equation given in Eq. (4) would lead to a significant over-estimation of dissolution rates ($\geqslant$ one order of magnitude) at near equilibrium conditions. These critical observations simply indicate that TST, which was originally developed for elementary reactions, is difficult to integrate into rate expressions that effectively represent a global dissolution process composed of multiple parallel and serial reactions.

4.4. Evolution of Si:Al stoichiometry and rates of dissolution with time and ΔG_r

4.4.1. Steady-state Si:Al stoichiometry

Here we examine the steady-state behavior of albite dissolution as a function of ΔG_r. The dissolution behavior is described in terms of the aqueous [Si]/[Al] stoichiometry (henceforth Si:Al), as well as R_{Si} and R_{Al}. Ratios of Si:Al = 2.7–3.0 are considered to represent albite stoichiometry (Hellmann, 1994; Harlow and Brown, 1980). Fig. 4 shows Si:Al as a function of ΔG_r for all experiments (see also Table 1), where Si:Al and ΔG_r are defined at the end of each experiment (or before a flow rate change in multiple flow rate experiments). Si:Al ratios from far-from-equilibrium experiments where either R_{Si} and R_{Al} exceeded the 1 SD criterion in Figs. 2A and B were excluded.

In the near equilibrium and transition equilibrium free energy regions ($-70 < \Delta G_r < 0$ kJ mol^{-1}), the majority of the Si:Al ratios are between 2.5 and 3.3, with an average of 2.83. Given the (low) uncertainties in the measured concentrations over this free energy range, we estimate that these data indicate stoichiometric steady-state dissolution. In the far-from-equilibrium free energy range ($\Delta G_r < -70$ kJ mol^{-1}) the data are evenly scattered about Si:Al = 2.7–3.0, with an average of 2.76. Given the large uncertainties in the measured Si and Al concentrations in this ΔG_r range, it is probable that analytical error is largely responsible for this apparent non-stoichiometry.

The results shown in Fig. 4 are in accord with several published studies. In a study by Hellmann (1995), steady-state albite dissolution at far-from-equilibrium conditions was stoichiometric at all temperatures (100, 200, and 300 °C) at basic pH (i.e., $R_{Si} \cong R_{Al}$). In the study by Burch et al. (1993), end-run Si:Al ratios of 2.87–3.71 over a ΔG_r

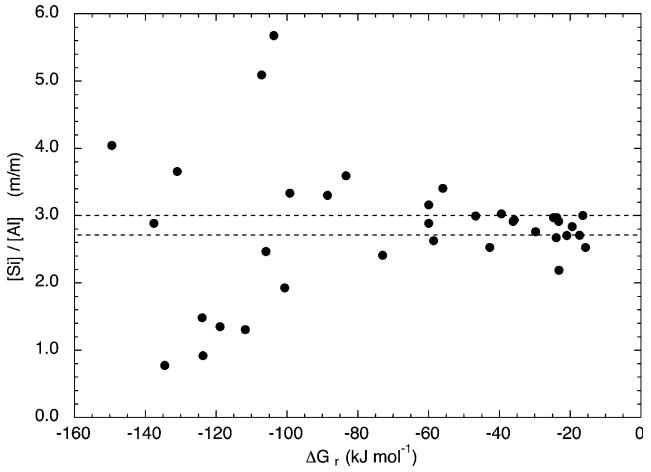

Fig. 4. [Si]:[Al] stoichiometry of solutions representing steady-state dissolution. Each datum represents the last sample of an experimental run, or in certain cases, the sample before a rate change occurred (see text). The region between the dashed lines represents Si:Al stoichiometry of unaltered albite (2.7–3.0). The ratios in the region $\Delta G_r \geqslant -70$ kJ mol^{-1} suggest stoichiometric behavior; the apparent non-stochiometric scatter at $\Delta G_r < -70$ kJ mol^{-1} is most probably due to analytical uncertainty in [Si] and [Al].

range of 0 to -44 kJ mol^{-1} were considered to represent stoichiometric albite dissolution. The results of Oelkers et al. (1994) show Si:Al ratios for albite ranging from 2.7 to 3.9 ($\Delta G_r < -28$ kJ mol^{-1}).

4.4.2. Non-steady-state Si:Al stoichiometry

Next we examine the temporal evolution of the Si:Al stoichiometry of albite dissolution for all experiments. The experiments have been grouped and compared according to the final ΔG_r attained. Even though the non-stoichiometric concentration ratios are discussed in terms of unequal release rates (i.e., $R_{Si} \neq R_{Al}$), this is only a simplification that may not be true, and should therefore not be construed to exclude other processes, as discussed at the end of this section.

In the far-from-equilibrium region ($-150 \leqslant \Delta G_r \leqslant -70$ kJ mol^{-1}), shown in Figs. 5A and B, the Si:Al ratios show two distinct asymmetric distributions about the stoichiometric ratio, depending on the ΔG_r range. Much of the observed non-stoichiometry can probably be attributed to analytical uncertainty, as is borne out by Fig. 1A, which shows both $R_{Si} > R_{Al}$ and $R_{Si} < R_{Al}$. However, the pronounced asymmetric nature of the two data sets may also point to a real phenomenon, confirmation of which would require detailed, high resolution surface analyses. These results are compared to a study by Hellmann (1995) who measured the time evolution of albite dissolution-stoichiometry at far-from-equilibrium conditions (R_{Si}, R_{Al}, R_{Na}; 100, 200, 300 °C, pH 12 ($pH_T = 10.3$, 9.3 and 9.3, respectively)). In that study the initial dissolution period was always non-stoichiometric: Si:Al > 3 at 100 °C, $\Delta G_r < -82$ kJ mol^{-1}; Si:Al < 3 at 200 °C, $\Delta G_r < -98$ kJ mol^{-1}; Si:Al $\ll$ 3 at 300 °C, $\Delta G_r < -101$ kJ mol^{-1}. These results support the observations in the present study, especially with respect to the change in stoichiometric behavior with decreasing ΔG_r (i.e., Si:Al > 3 → Si:Al < 3), and therefore suggest that ΔG_r and Si:Al are dependent on each other during the initial, non-steady-state phase of dissolution.

The approach to steady-state rates in the transition equilibrium free energy range ($-70 \leqslant \Delta G_r \leqslant -25$ kJ mol^{-1}) is characterized by low to moderate non-stoichiometric behavior, with Si:Al ratios ranging from ≈3.4 to 2.7 (based on 10 experiments, see Fig. 5C). However, a few experiments show the opposite behavior (e.g., see Fig. 1B). Many of the experiments display a small degree of non-stoichiometric behavior in the non-steady-state phase, followed by 'approximate' stoichiometric steady-state dissolution characterized by Si:Al ≈ 3.3–3.4; others achieve steady state with 'true' stoichiometric behavior, yielding Si:Al ratios ranging from 2.7 to 3.0. Whether these differences are real or simply due to analytical uncertainties is difficult to assess. Similar behavior can be extrapolated from data (with equivalent range of ΔG_r) reported in Burch et al. (1993), where the initial stages of dissolution ($\Delta G_r = -27$ kJ mol^{-1}) are roughly stoichiometric (Si:Al ≈ 3.0: Expt. AD11, Fig. 2) or moderately non-stoichiometric (Si:Al ≈ 3.6, Expt. AD6, Fig. 4).

While the final, steady-state rates are nearly all stoichiometric in the near equilibrium free energy range ($-25 < \Delta G_r < 0$ kJ mol^{-1}), some of the experiments display a significant degree of non-stoichiometric behavior, characterized by Si:Al < 2.7, as shown in Fig. 5D (data shown include Si:Al ratios from multiple flow rate experiments). The observed non-stoichiometric behavior, due to $R_{Al} > R_{Si}$, typically occurs during the non-steady-state, initial phase of each experiment, or after a flow rate change. This non-stoichiometry appears to be real since analytical errors can be largely excluded as a cause (i.e., [Si], [Al] in ppm range, low analytical uncertainty). Interestingly, at conditions close to equilibrium, some of the initial data in Burch et al. (1993) show Si:Al ≈ 9.6 (Expt. AD20, Fig. 3 therein).

To summarize, the data from the present study reveal that ΔG_r not only controls steady-state rates of dissolution, but also influences the stoichiometric behavior of the initial, non-steady-state period of dissolution. The predominant trend displayed by pre-steady-state data at conditions far from equilibrium is characterized by Si:Al < 2.7. However, this trend is reversed over the range $-110 \leqslant \Delta G_r \leqslant -25$ kJ mol^{-1}, where Si:Al $\geqslant$ 3.0. And finally, at conditions close to equilibrium, the data show non-steady-state rates with Si:Al $\leqslant$ 2.7. Nonetheless, more work is necessary to confirm and expand upon these non-steady-state results, and in particular, at dissolution conditions far from equilibrium. It is possible that the non-stoichiometry of [Si]/[Al] is due to the 'classical' argument related to $R_{Si} \neq R_{Al}$ and the formation of leached layers (Hellmann, 1995; Hellmann et al., 1997; and references therein). However, this non-stoichiometry may just as well point to other processes, such as interfacial dissolution–reprecipitation (Hellmann et al., 2003), or precipitation of

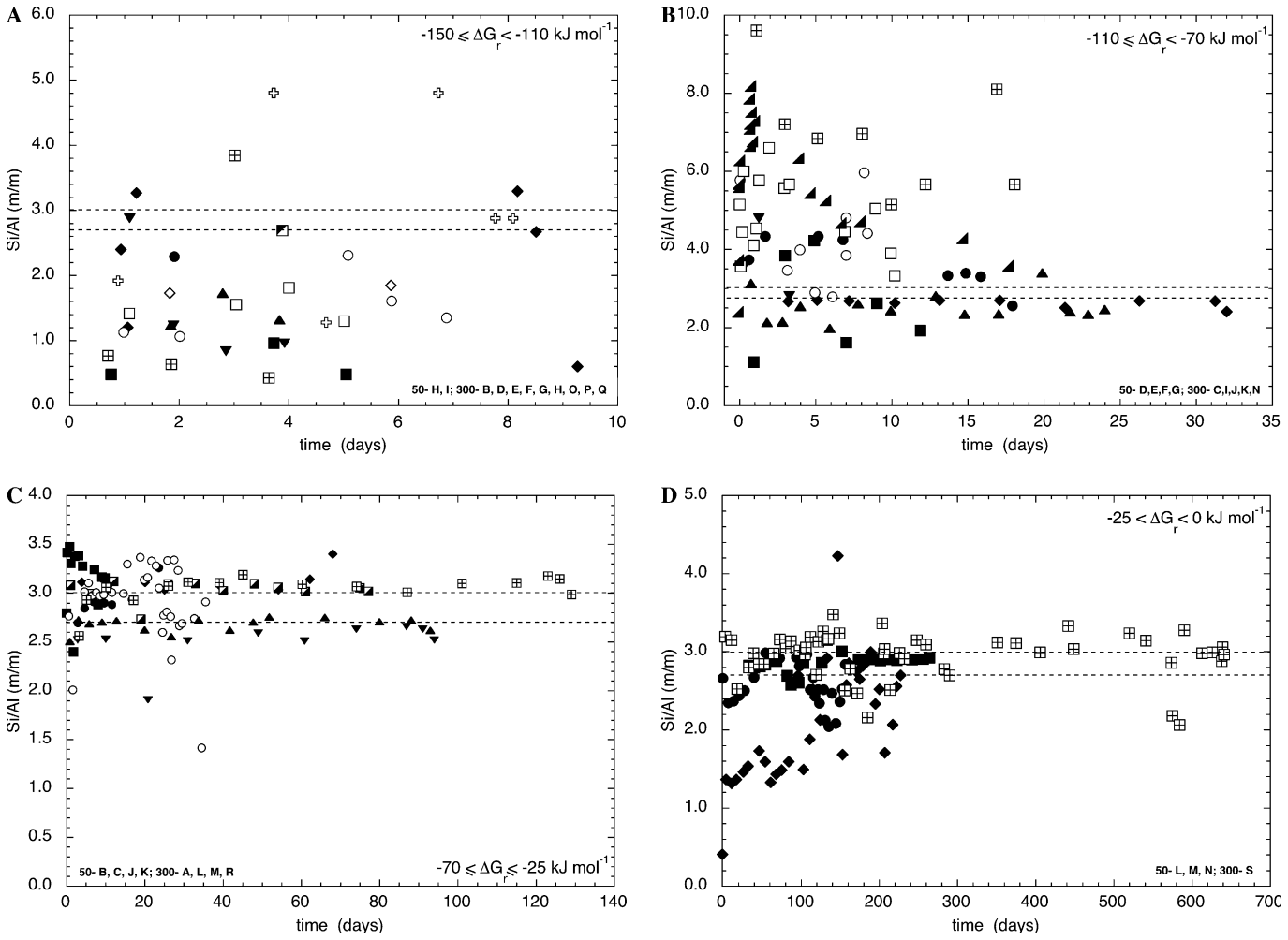

Fig. 5. Non-steady-state temporal evolution of [Si]:[Al] stoichiometry for all experiments, with comparisons among data sets (indicated by different symbols, but not defined) based on four free energy ranges. Region between dashed lines represents unaltered albite Si:Al stoichiometry. The overall results indicate that ΔG_r influences the stoichiometry of non-steady-state dissolution. (A) At far-from-equilibrium conditions, $-150 \leqslant \Delta G_r < -110$ kJ mol^{-1}, [Si]:[Al] < 2.7 (data with high analytical uncertainty). (B) Over free energy range $-110 \leqslant \Delta G_r < -70$ kJ mol^{-1}, [Si]:[Al] > 3.0 (data with moderate analytical uncertainty). (C) In transition equilibrium range, $-70 \leqslant \Delta G_r \leqslant -25$ kJ mol^{-1}, [Si]:[Al] $\approx$ 3.4 to 2.7; over longer time periods ($t > 40$ days), [Si]:[Al] $\approx$ albite. (D) At near equilibrium, $-25 < \Delta G_r < 0$ kJ mol^{-1}, some experiments display significant non-stoichiometric behavior, Si:Al < 2.7, occurring during initial dissolution, or after a flow rate change. Long term ($t > 250$ days) behavior shows [Si]:[Al] $\approx$ albite.

secondary phases from an oversaturated bulk solution. The latter possibility is treated next.

4.5. Precipitation of secondary phases

4.5.1. SEM images

As dissolution conditions approach equilibrium, the possible formation of secondary phases due to bulk solution oversaturation and precipitation, is always a distinct possibility. Based on the measured solution compositions, EQ3NR (Wolery, 1992) was used to determine ΔG_r values with respect to the formation of secondary phases. As shown in Table 2, the formation of two potential secondary phases (analcime: $NaAlSi_2O_6 \cdot H_2O$ and natrolite: $Na_2Al_2Si_3O_{10} \cdot 2H_2O$) was thermodynamically feasible in those experiments where $\Delta G_r \geqslant -25$ kJ mol^{-1}. To avoid confusion in the following discussion, ΔG_r always refers to albite dissolution; ΔG_r for reactions concerning other phases is subscripted accordingly.

To confirm whether secondary phases formed on albite grain surfaces during the dissolution runs, a large number of post-reaction samples were imaged with secondary electrons using scanning electron microscopy (SEM). One to two random grains were used from a few representative experiments, and for each grain surface, multiple randomly chosen areas on different cleavage surfaces were imaged. The following list indicates the experiment, the maximum ΔG_r in kJ mol^{-1}, and the number of grains imaged (if more than one): 50 N (−16); 50 L (−19) (2); 300 S (−21) (2); 300 A (−30); 50 K (−39) (2); 300 M (−43); 300 K (−73); 50 D (−83); 300 O (−131) (2); 300 D (−134); 50 I (−140) (2).

On nearly all samples reacted at $\Delta G_r < -25$ kJ mol^{-1}, and after numerous surface SEM scans at high magnification (>10,000×), it was nearly always possible to document

Table 2
Gibbs free energy of reaction for albite and secondary phases

Expt.	ΔG_r (albite) (kJ mol^{-1})	ΔG_r (analcime) (kJ mol^{-1})	ΔG_r (natrolite) (kJ mol^{-1})
50 L-20	−23.86	−0.40	−4.77
50 L-35	−19.27	+2.99	+0.77
50 M-25	−23.11	+0.11	−4.06
50 N-15	−15.55	+5.86	+5.69
50 N-25	−16.33	+5.15	+4.27
50 N-31	−17.25	+4.54	+3.40
300 S-15	−23.64	−0.31	−60.14
300 S-61	−20.81	+1.88	−1.00
300 S-85	−23.07	+0.34	−3.26
300 S-92	−24.58	−1.01	−5.94

an isolated occurrence of what appeared to be a micro-secondary crystalline phase. These rare and very isolated phases always occurred at the bottom of etch pits, in micro-cracks, pores, etc. This is evidence that secondary phases can form on grains dissolved over a wide range of ΔG_r (including far-from-equilibrium conditions and bulk solution undersaturation with respect to all secondary phases) in special micro-surface environments that harbor stagnant fluids; such fluids can attain degrees of saturation far greater than the surrounding bulk fluid. However, given their isolated and very rare nature, these precipitates are unimportant to the overall dissolution process. Samples reacted at $\Delta G_r > -25$ kJ mol^{-1} (expts. 50 L, 50 M, 50 N, 300 S) displayed more ample evidence for the presence of surface precipitates; two experiments are examined in detail.

SEM images of one of the grains recovered from experiment 50 N (227 days of reaction, $\Delta G_{r\,\max} = -16$ kJ mol^{-1}) are shown in Figs. 6A–E (Figs. 6A–C, and D–E are 2 series of nested, sequential images). Fig. 6A shows a very rounded grain, with a very irregular and pitted surface topography. Figs. 6A and B also reveal the presence of numerous irregular and blocky fragments, up to ~20 μm in size. Energy dispersive X-ray analysis (EDX) did not produce meaningful results since the volume of analysis and electron spot size were too large for such small objects. They most probably represent extraneous albite fragments, and not secondary precipitates. Fig. 6B reveals that the surface topography consists of irregular, blocky terraces and depressions in combination with what appear to be etch pits; note also the large population of much smaller (~1–5 μm) etch pits with a distinct trigonal (pyramidal?) geometry. Very similar irregular topography and pitting were also observed on 2 grains from experiment 50 L (157 days reaction, $\Delta G_{r\,\max} = -19$ kJ mol^{-1}). Fig. 6C shows a terrace with extraneous fragments, and more importantly, the presence of barely visible, non-connected platy precipitates ($\phi \ll 1$ μm).

Some surface regions, consisting exclusively of prominent surface depressions, did reveal the presence of massive surface precipitates, as shown in Fig. 6D. An image at higher magnification, see Fig. 6E, shows that the precipitate is made of platy crystal masses. Even though the surface coverage of crystals is extensive in Fig. 6E, substantial porosity exists, suggesting that the crystal aggregate should not have impeded fluid and mass transfer between the dissolving surface and the bulk fluid. Qualitative EDX analyses of the extensive lateral crystal 'mats' yielded elemental spectra virtually identical to that of adjacent albite surfaces not covered by crystals. However, as mentioned before, the SEM-EDX approach is not adapted for this scale of analysis, especially since the depth of surface coverage of crystals is probably thin. Similar restricted occurrences of massive precipitates were also observed on grains from experiment 50 L. We should emphasize at this point that the overall nature of the grain surfaces examined from 50 N and 50 L resembles those shown in Figs. 6A–D, whereas massive precipitates (Fig. 6E) only occurred in restricted areas characterized by prominent surface depressions (constituting perhaps <5% of the total surface).

Table 2 indicates that the aqueous solutions from experiments 50 N and 50 L had the highest positive values for $\Delta G_{r\,\text{analcime}}$ and $\Delta G_{r\,\text{natrolite}}$ recorded in this study. Whether or not these two phases constitute the precipitates shown in Figs. 6C and E could not be verified, and would require more sophisticated methods of microanalysis (e.g., HRTEM). Moreover, the estimation of ΔG_r for supersaturated phases does not preclude the formation of other secondary phases (including albite) at conditions close to equilibrium, given the fact that only the bulk solution chemistry can be measured, and not the chemistry of fluids in surface depressions, etch pits, micropores, etc. In addition, estimates of solution supersaturation do not yield information on another important parameter, the kinetics of crystallization of secondary phases.

The second case examined is based on two grains from experiment 300 S (641 days reaction, $\Delta G_{r\,\max} = -21$ kJ mol^{-1}). While the difference in $\Delta G_{r\,\max}$ is only ~−5 kJ mol^{-1} compared to 50 N, these grains are remarkably different. They reveal surfaces characterized by a dense coverage of prismatic etch pits, with none of the irregular surface pitting and topography evidenced in Figs. 6A, B, and D. A SEM image (Fig. 7A) of a typical surface shows extensive etch pit development, consisting of large etch pits (up to 70 μm in diameter), as well as a large population of smaller etch pits, with diameters to 10 μm. At the scale of observation shown in Fig. 7A, no evidence for massive surface precipitation was noted on both grains. At a higher scale of magnification, the etch pits show a regular geometry governed by distinct angles and planar pit walls, as seen in Fig. 7B (this is also in contrast to irregular pits seen on 50 N and 50 L). The bottoms of many of the smaller etch pits contain isolated clusters of small secondary crystal aggregates; these have a morphological resemblance with the crystal aggregates in Fig. 6E. As shown in Table 2, only analcime was thermodynamically favored to form in 300 S; note that $\Delta G_{r\,\text{analcime}}$ is lower for 300 S compared to 50 N and 50 L. This small difference is apparently the reason why precipitates are rare in 300 S, and more prevalent in 50 N and 50 L.

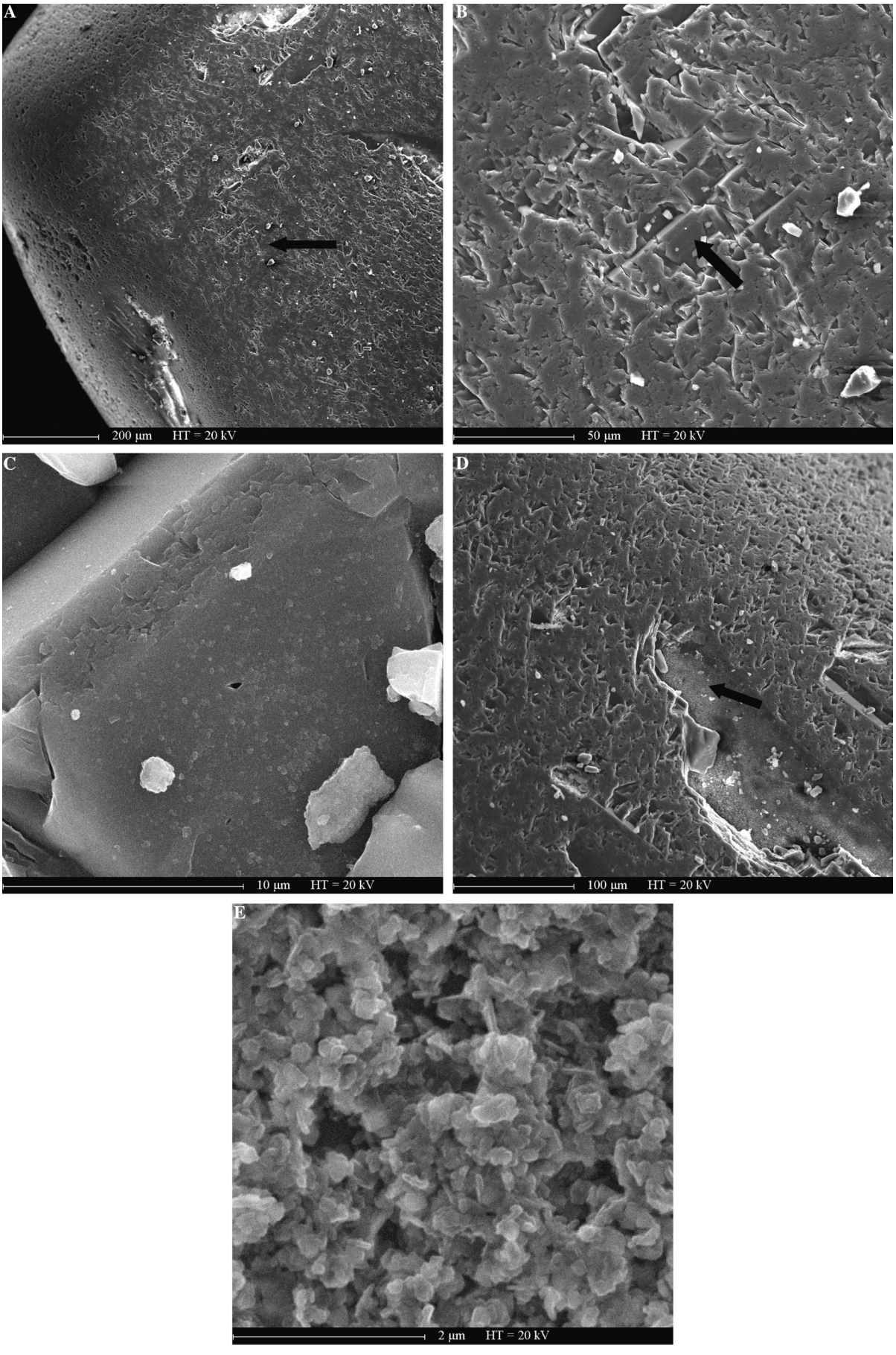
A
200 µm HT = 20 kV
B
50 µm HT = 20 kV
C
10 µm HT = 20 kV
D
100 µm HT = 20 kV
E
2 µm HT = 20 kV

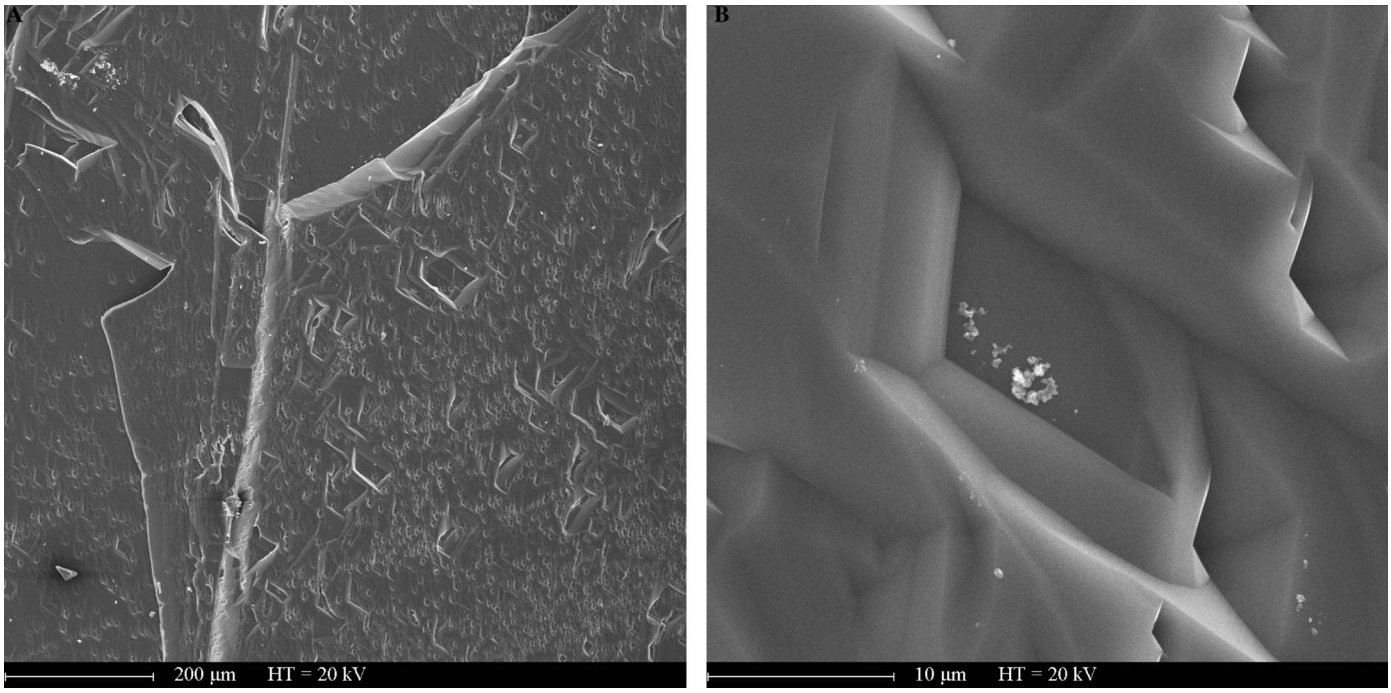

Fig. 7. SEM images of grain surface from experiment 300 S (641 days reaction, $\Delta G_{r\ \max} = -21$ kJ mol^{-1}). (A) Surface is extensively covered with large, prismatic etch pits (up to 70 µm in diameter), as well as a large population of smaller etch pits, with diameters to 10 µm. None of the irregular surface dissolution features evidenced in Figs. 6A–D was observed. No evidence for massive surface precipitation was noted (as in Figs. 6D–E). (B) Image at higher magnification reveals that etch pit bottoms frequently contain isolated clusters of small secondary crystal aggregates. The morphology of these aggregates is similar to Fig. 6E, but with vastly inferior surface coverage. Comparing experiments 50 N and 300 S, the small difference in ΔG_r (Table 2) played a significant role in the amount of secondary phases that formed (see Table 2).

In summary, a comparison of the results between 50 N (and 50 L) with 300 S point out that a small difference in ΔG_r can have an important impact on the dissolution process, especially as related to etch pit and surface topography development. Moreover, this ΔG_r interval from -16 to -21 kJ mol^{-1} (50 N vs. 300 S) coincides with a specific range in ΔG_r that marks the boundary between the near equilibrium and the transition equilibrium regime, localized at approximately -17 to -25 kJ mol^{-1} (Figs. 3A and B). Thus, at the higher ΔG_r boundary (50 N), surface edges are rounded and pitting is very irregular, and at the lower ΔG_r boundary (300 S), surface edges are sharp and etch pits are perfectly prismatic. This may be evidence for a ΔG_r-dependent change in reaction mechanism. However, one caveat should be considered—surfaces continuously evolve during an experiment as they re-equilibrate with the ambient ΔG_r, and the time required may exceed the time of the experimental run. Therefore, some of the etch pitting and surface topography features observed (50 N, 300 S) may be vestiges of antecedent free energy conditions that are not completely representative of $\Delta G_{r\ \text{final}}$.

Another very important point, interrelated with the surface topography-ΔG_r dependence, is that the free energy range -17 to -25 kJ mol^{-1} is characterized by a significant change in rate behavior (Figs. 3A and B). This is compatible with BCF theory (Cabrera and Levine, 1956; van der Hoek et al., 1982) that predicts the existence of a critical free energy value, ΔG_r^{crit}, defined to be the energy needed for etch pits to spontaneously open up and grow. This theory has been applied to mineral dissolution kinetics, and in particular has been used to explain the sharp change in the R–ΔG_r relation, which is attributed to a switch occurring at ΔG_r^{crit} between two different rate-controlling dissolution mechanisms (for details, see Lasaga and Blum, 1986; Brantley et al., 1986; Blum et al., 1990; Burch et al., 1993; Lasaga and Lüttge, 2001, 2003). Experimental evidence supporting this is the main reason why an additive, two-mechanism dissolution rate law was used by Burch

Fig. 6. SEM images of grain from experiment 50 N (227 days of reaction, $\Delta G_{r\ \max} = -16$ kJ mol^{-1}). 50 N represents dissolution conditions closest to equilibrium; EQ3NR (Wolery, 1992) calculations indicate that formation of analcime and natrolite was thermodynamically possible. (A) Well rounded grain with irregular and pitted surface topography. Arrow indicates area enlarged in next image. (B) Surface topography consists of irregular, blocky terraces and depressions in combination with what appear to be large, irregular-shaped etch features. Note also significant population of much smaller (~1–5 µm) etch pits with distinct trigonal geometry. Large foreign objects are probably extraneous albite fragments. Arrow indicates area enlarged in next image. (C) Terrace covered by barely visible surface precipitates (<1 µm) in the form of single platy crystals. The foreign objects are either albite fragments and/or aggregates of secondary precipitates. (D) Prominent topographic depression (visible in upper right corner of Fig. 6A) covered by laterally extensive secondary precipitates (total surface coverage ~ < 5%). Arrow indicates area enlarged in next image. (E) Highly magnified image revealing that precipitate is made of aggregate of platy crystals; substantial porosity probably remains. SEM-EDX analyses were unable to identify phase.

et al. (1993). Similarly, the nature of the R–ΔG_r relation and the surface topography observations presented in this study also support this theory, and therefore the Burch et al. (1993) approach was adapted via Eq. (9).

4.5.2. Did secondary phase formation affect the R–ΔG_r relation?

Precipitation of a secondary phase can change both the apparent rate of dissolution and the calculated free energy by changing the concentrations of the released elements in the bulk solution; in this study the elements are Na, Al, and Si. Two predominant mechanisms that can cause this are the incorporation of Na, Al, and/or Si into a secondary phase, and/or adsorption of these elements onto surface sites (either existing or newly created). Note that the elemental dissolution rates $R_{\mathrm{Si,\,Al}}$ are more susceptible to change (higher sensitivity) than ΔG_r as a consequence of secondary precipitation and/or adsorption processes, as can be deduced from the mathematical expressions that define these parameters (i.e., compare Eq. (5) to $\Delta G_r = \mathrm{R}T \ln(Q/K_{\mathrm{eq}})$).

One of the principal criteria for evaluating the effect of a precipitate is based on its surface coverage as a function of the total surface area of the dissolving mineral. In the present study, for all experiments where $\Delta G_{r\,\max} < -25$ kJ mol^{-1}, the ratio of surface precipitate area to the total surface area of dissolving albite is extremely small, based on representative SEM images of grain surfaces. When $\Delta G_{r\,\max} > -25$ kJ mol^{-1}, the surface area ratios are also deemed not important. For experiment 300 S ($\Delta G_{r\,\max} = -21$ kJ mol^{-1}), the total surface coverage by secondary phases present is negligible, as evidenced by the representative SEM image in Fig. 7B. Experiments 50 N and 50 L represent dissolution conditions that most closely approached equilibrium ($\Delta G_{r\,\max} = -16$ and -19 kJ mol^{-1}, respectively), and even in these cases, it is estimated that extensive surface precipitates (located in depressions) cover no more than 5% of the total surface, as discussed earlier. In addition, as supported by Fig. 7B, the crystal aggregates appear to be porous and probably did not affect the transfer of fluids and dissolved constituents between the bulk fluid and the dissolving surface. To lend support to the idea that the precipitates observed in this study had a negligible effect on the rates of dissolution, we discuss three lines of evidence.

The first reason is based on the measured rates of experiments 50 L, 50 M, 50 N, and 300 S. In Fig. 3A and B, these experiments are all clustered in R–ΔG_r space ($-25 < \Delta G_r < -15$ kJ mol^{-1}), and given the scatter in these rates with respect to the fitted R–ΔG_r relation, we estimate that the differences are not statistically significant. As an example, a comparison of R_{Si} and R_{Al} for 300 S (grain surfaces virtually free of precipitates) and 50 L (grain surfaces with precipitates) shows the respective rates to be almost identical (within ± 1 SD, see Table 1). Second, no discernible (decreasing) trends in $\overline{R}$ are noted. Fig. 8 shows the time evolution of the rates of dissolution for experiment

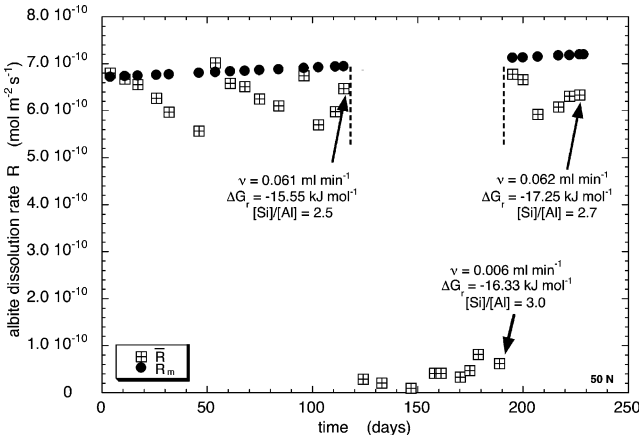

Fig. 8. Time evolution of dissolution rates, experiment 50 N: 229 days, three flow rate regimes, $\Delta G_{r\ \max} = -16$ kJ mol^{-1}. Since there is no discernible trend in $\overline{R}$ over the course of the experiment (excluding intermediate flow regime), and based on the variability of $\overline{R}$, it appears that formation of secondary precipitates (e.g., Figs. 6D and E) did not lead to any discernable changes in the rate of dissolution. Note also that the indicated steady-state ratios [Si]/[Al] do not change in a systematic way with time, also indicating that there was no significant effect due to secondary phase precipitation.

50 N. Over the 229-day period of the experiment, there is no discernible trend in $\overline{R}$ ($v = 0.061$ ml min^{-1}), with $\overline{R}_{\mathrm{start}} = 6.80 \times 10^{-10}$ and $\overline{R}_{\mathrm{end}} = 6.34 \times 10^{-10}$mol m^{-2} s^{-1} (refer to Fig. 8). Moreover, the difference in $\overline{R}$ is less than the measured variations of $\overline{R}$ during the initial and terminal flow regimes of the experiment. The temporal evolution of $\overline{R}$ for the other experiments with observed precipitates, i.e., 50 L, 50 M, 300 S- see Table 2, also did not show any decreasing trends in $\overline{R}$. Third, the ratio [Si]/[Al], calculated at specific time intervals, does not change in a systematic way, as shown in Fig. 8. Had analcime or natrolite precipitation been responsible for a significant change in the dissolution process, [Si]/[Al] should have diverged in a systematic manner from 3.0, but this was not measured (note: this argument only holds if the precipitate phase has a different [Si]/[Al] ratio than albite). In summary, we conclude that the formation of precipitates at near equilibrium conditions had no perceptible influence on the measured rates, and by inference, on the R–ΔG_r relation.

5. Conclusions

The most important result of this study is an extensive and continuous set of data relating the dissolution rate of albite feldspar as a function of the free energy of reaction. The data are highly non-linear and show a sigmoidal relation between R and ΔG_r, which precludes a classical TST model to interpret the results. This is one of the few studies to provide much needed data in the transition equilibrium region. Equally important is the fact that the data conclusively show the existence of an extended dissolution rate plateau starting at $\sim\Delta G_r < -70$ kJ mol^{-1} and extending

to at least -150 kJ mol^{-1}. The existence of a rate plateau is conceptually very important in that it reveals the existence of a free energy range where the dissolution rate remains constant and independent of ΔG_r, and consequently also independent of [Si] and [Al] in solution. The sigmoidal behavior of the rates as a function of ΔG_r in the present study indicates a non-linear approach to equilibrium. The issue of how rates approach equilibrium is of crucial importance since this is the basis of R–ΔG_r models, which of course are of key importance in the extrapolation of experimental results to the field scale.

The rate data in the present study extend to $\Delta G_r = -15.6$ kJ mol^{-1}. At present, experiments are underway that examine the R–ΔG_r relation at dissolution conditions much closer to equilibrium, in the range $-15 < \Delta G_r < 0$ kJ mol^{-1}. This will allow us to obtain a more complete data set and will help better define the dependence of the dissolution rate on the free energy in the immediate vicinity of equilibrium. As will be shown in an upcoming study, there is an overall lack of rate data in the literature associated with $\Delta G_r > -5$ kJ mol^{-1}, and therefore, this will be an area of fruitful research in the future. However, experimentation will almost certainly be challenging due to the complexities associated with unraveling the dissolution rate signal from the effects of highly likely secondary phases.

In addition to secondary phase formation, the question of how the microtopography, as well as the structure and chemistry of the surface and near surface, evolve as a function of free energy (see e.g., labradorite near-surface study by Hellmann et al., 2003) need to be examined. Observing and measuring the dissolution process at the nano-scale, and understanding its relation to macroscopic data from reactor-based studies (such as the present study) will be an important endeavor to undertake in order to more fully unravel the complexities of the R–ΔG_r relation and the overall dissolution mechanism.

Acknowledgments

This project was funded by the following programs: Arc Géothermie du PIRSEM, Arc Géothermie des Roches Fracturées, DBT II-INSU "Fluides dans la Croûte", ECODEV, EC contract ENK5-2000-00301 (years 2001–2004), EGS Pilot Plant EC contract SES-CT-2003-502706 (years 2005–present). We thank Damien Faivre (ENS-Lyon) for assistance with experimental work during a summer internship. The high quality SEM images were taken by Sebastien Pairis (Laboratoire de Cristallographie, CNRS Grenoble). Informal comments by Jeremy Fein, and formal reviews by Sue Brantley, Don Rimstidt, Andreas Lüttge, an anonymous reviewer, and (AE) David Wesolowski were much appreciated and helped improve the manuscript.

Associate editor: Dave Wesolowski

Appendix A

One of the particularities of this study was the significant difference in experimental time spans for each experiment, which ranged from 4 to 5 days at far-from-equilibrium conditions to 641 days at near equilibrium conditions. Even though relatively constant [Si] and [Al] were measured at the end of all experiments, this in a few cases did not translate to the establishment of steady-state rates for R_{Si} and R_{Al}. As already discussed (Section 3.3.1), the culprit causing this problem was the use of a constant specific surface area SSA for the calculation of dissolution rates. More specifically, this caused the estimated total surface area (SSA · sample mass $m(t)$) to decrease with time for each experiment. This approximation had no noticeable effect on short-term experiments (e.g., Fig. 1A) and most intermediate to long-term experiments, as evidenced by the achievement of steady-state rates. However, with respect to a few experiments, R_{Si} and R_{Al} did not stabilize and become constant after the initial, non-steady-state phase of dissolution. This artifact was most apparent in the unrealistic behavior of R_m which monotonically increased with time (we note two examples showing $R_{m\ final} > R_{m\,initial}$: Fig. 1B: 12% increase; Fig. 1C: 33% increase).

As a first approximation solution to this problem, we applied a normalization procedure to measured rates based on the assumption that R_m should remain constant during a given experiment. This condition can be met if the linear loss in sample mass is balanced by a linear increase in SSA with time, due to etch pit formation and growth, formation of internal surface structures (mesopores/micropores, e.g., Anbeek, 1992), dissolution step waves (Lüttge et al., 2003), etc. This approach does not correctly account for initial dissolution rates that are higher or lower than stea-

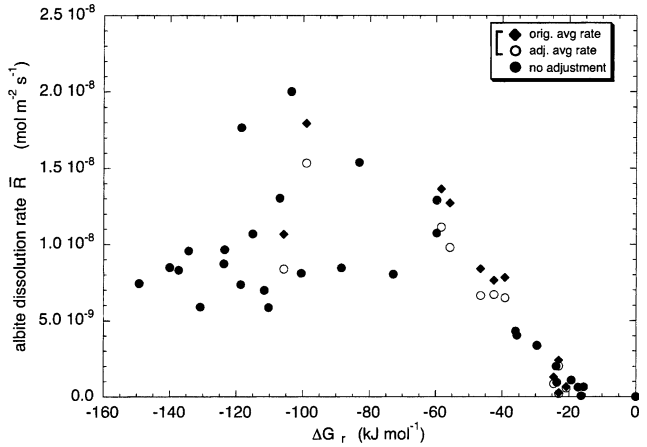

Fig. 9. Dissolution rate $\overline{R}$ as function of ΔG_r, showing original and adjusted rates based on adjustment procedure described in Appendix A. While the majority of the rates were not adjusted (solid black circles), 10 rates were adjusted by factors ranging from 0.88 to 0.67. Note that the overall effect of the rate adjustments on the $\overline{R}$–ΔG_r relation is not significant.

dy-state rates, but it is, nonetheless, a reasonable method for treating the overall long-term evolution of surface areas in this study (Grandstaff, 1978; Zhang et al., 1993; Gautier et al., 2001; Mellott et al., 2002).

The adapted normalization procedure was applied according to the measured change in R_m over the course of each experiment. When $R_{m\,initial}/R_{m\,final} \geqslant 0.90$, no correction was applied, as we deemed it better to leave the original rate untreated. On the other hand, when $R_{m\,initial}/R_{m\,final} < 0.90$, $\overline{R}$ was decreased by a factor equal to $R_{m\,initial}/R_{m\,final}$. This normalization routine was only applied to (terminal) average rates $\overline{R}$ (Fig. 3), and not to the original R_{Si}, R_{Al}, and R_m rates shown in Figs. 2A–C. Overall, the majority of $\overline{R}$ in this study were not adjusted, but ten rates were decreased by factors ranging from 0.88 to 0.67 (mean adjustment factor = 0.80). Fig. 9 shows the original and adjusted values of $\overline{R}$; note that the overall effect of the rate adjustments on the $\overline{R}$–ΔG_r relation is not significant.

References

Aagaard, P., Helgeson, H.C., 1977. Thermodynamic and kinetic constraints on the dissolution of feldspars (abs.). *Geol. Soc. America Abs. w. Programs* **9**, 873.

Aagaard, P., Helgeson, H.C., 1982. Thermodynamic and kinetic constraints on reaction rates among minerals and aqueous solutions. I. Theoretical considerations. *Am. J. Sci.* **282**, 237–285.

Alekseyev, V.A., Medvedeva, L.S., Prisyagina, N.I., Meshalkin, S.S., Balabin, A.I., 1997. Change in the dissolution rates of alkali feldspars as a result of secondary mineral precipatation and approach to equilibrium. *Geochim. Cosmochim. Acta* **61**, 1125–1142.

Anbeek, C., 1992. Surface roughness of minerals and implications for dissolution studies. *Geochim. Cosmochim. Acta* **56**, 1461–1469.

Beig, M.S., and Lüttge, A., 2005. Near-equilibrium albite dissolution kinetics. *Geochim. Cosmochim. Acta Special Supplement, Abs. 15th Ann. Goldschmidt Conf.*, 69, A780.

Beig, M.S., and Lüttge, A., 2006. Albite dissolution kinetics as a function of distance from equilibrium: implications for natural feldspar weathering, *Geochim. Cosmochim. Acta*, **70**, in press.

Bénézeth, P., Palmer, D., Wesolowski, D.J., 2001. Aqueous high-temperature solubility studies. II. The solubility of boehmite at 0.03 m ionic strength as a function of temperature and pH as determined by in situ measurements. *Geochim. Cosmochim. Acta* **65**, 2097–2111.

Berger, G., 1995. The dissolution rate of sanidine between 100 and 300 °C. In: Kharaka, Y.K., Chudaev, O. (Eds.), *Water–Rock Interaction WRI-8, Vol. WRI-8*. Balkema, Amsterdam, pp. 141–144.

Berger, G., Beaufort, D., Lacharpagne, J.-C., 2002. Experimental dissolution of sanidine under hydrothermal conditions: Mechanism and rate. *Am. J. Sci.* **302**, 663–685.

Blum, A.E., Yund, R.A., Lasaga, A.C., 1990. The effect of dislocation density on the dissolution rate of quartz. *Geochim. Cosmochim. Acta* **54**, 283–297.

Blum, A.E., Stillings, L.L., 1995. Feldspar dissolution kinetics. In: White, A.F., Brantley, S.L. (Eds.), *Chemical Weathering Rates of Silicate Minerals*, Vol. 31. Mineralogical Society of America, pp. 291–351.

Brantley, S.L., Mellott, N.P., 2000. Surface area and porosity of primary silicate minerals. *Amer. Mineral.* **85**, 1767–1783.

Brantley, S.L., White, A.F., Hodson, M.E., 1999. Surface area of primary silicate minerals. In: Jamtveit, B., Meakin, P. (Eds.), *Growth, Dissolution and Pattern Formation in Geosystems*. Kluwer Academic Publishers, Dordrecht, pp. 291–326.

Brantley, S.L., Crane, S.R., Crerar, D.A., Hellmann, R., Stallard, R., 1986. Dissolution at dislocation etch pits in quartz. *Geochim. Cosmochim. Acta* **50**, 2349–2361.

Burch, T.E., Nagy, K.L., Lasaga, A.C., 1993. Free energy dependence of albite dissolution kinetics at 80 °C and pH 8.8. *Chem. Geol.* **105**, 137–162.

Cabrera, N., Levine, M.M., 1956. On the dislocation theory of evaporation of crystals. *Phil. Mag.* **1**, 450–458.

Casey, W.H., Westrich, H.R., Massis, T., Banfield, J.F., Arnold, G.W., 1989. The surface of labradorite feldspar after acid hydrolysis. *Chem. Geol.* **78**, 205–218.

Chou, L., Wollast, R., 1985. Steady-state kinetics and dissolution mechanisms of albite. *Am. J. Sci.* **285**, 963–993.

Drever, J.I., Clow, D.W., 1995. Weathering rates in catchments. In: White, A.F., Brantley, S.L. (Eds.), *Chemical Weathering Rates of Silicate Minerals*, Vol. 31. Mineralogical Society of America, pp. 463–483.

Drever, J.I., Murphy, K.M., Clow, D.W., 1994. Field weathering rates versus laboratory dissolution rates: an update. *Mineralogical Magazine* **58A**, 239–240.

Gautier, J.-M., Oelkers, E.H., Schott, J., 2001. Are quartz dissolution rates proportional to B.E.T. surface areas? *Geochim. Cosmochim. Acta* **65**, 1059–1070.

Gautier, J.-M., Oelkers, E.H., Schott, J., 1994. Experimental study of K-feldspar dissolution rates as a function of chemical affinity at 150 °C and pH 9. *Geochim. Cosmochim. Acta* **58**, 4549–4560.

Grandstaff, D.E., 1978. Changes in surface area and morphology and the mechanism of forsterite dissolution. *Geochim. Cosmochim. Acta* **42**, 1899–1901.

Harlow, G.E., Brown Jr., G.E., 1980. Low albite: an X-ray and neutron diffraction study. *Amer. Mineral.* **65**, 986–995.

Hellmann, R., 1994. The albite-water system: Part I. The kinetics of dissolution as a function of pH at 100, 200, and 300 °C. *Geochim. Cosmochim. Acta* **58**, 595–611.

Hellmann, R., 1995. The albite-water system Part II. The time-evolution of the stoichiometry of dissolution as a function of pH at 100, 200 and 300 °C. *Geochim. Cosmochim. Acta* **59**, 1669–1697.

Hellmann, R., Dran, J.-C., Della Mea, G., 1997. The albite-water system Part III. Characterization of leached and hydrogen-enriched layers formed at 300 °C using MeV ion beam techniques. *Geochim. Cosmochim. Acta* **61**, 1575–1594.

Hellmann, R., Penisson, J.-M., Hervig, R.L., Thomassin, J.-H., Abrioux, M.-F., 2003. An EFTEM/HRTEM high-resolution study of the near surface of labradorite feldspar altered at acid pH: evidence for interfacial dissolution-reprecipitation. *Phys. Chem. Minerals* **30**, 192–197.

Holdren Jr, G.R., Speyer, P.M., 1987. Reaction rate-surface area relationships during the early stages of weathering. II. Data on eight additional feldspars. *Geochim. Cosmochim. Acta* **51**, 2311–2318.

Komninou, A., Yardley, B.W.D., 1997. Fluid-rock interactions in the Rhine Graben: a thermodynamic model of the hydrothermal alteration observed in deep drilling. *Geochim. Cosmochim. Acta* **61**, 515–531.

Lasaga, A.C., 1981. Transition state theory. In: Lasaga, A.C., Kirkpatrick, R.J. (Eds.), *Kinetics of Geochemical Processes*, Vol. 8. Mineralogical Society of America, pp. 135–169.

Lasaga, A.C., 1984. Chemical kinetics of water–rock interactions. *J. Geophys. Res.* **89**, 4009–4025.

Lasaga, A.C., 1995. Fundamental approaches in describing mineral dissolution and precipitation rates. In: White, A.F., Brantley, S.L. (Eds.), *Chemical Weathering Rates of Silicate Minerals*, Vol. 31. Mineralogical Society of America, pp. 23–86.

Lasaga, A.C., 1998. *Kinetic Theory in the Earth Sciences*. Princeton University Press, New Jersey.

Lasaga, A.C., Blum, A.E., 1986. Surface chemistry, etch pits and mineral-water interactions. *Geochim. Cosmochim. Acta* **50**, 2363–2379.

Lasaga, A.C., Lüttge, A., 2001. Variation of crystal dissolution rate based on a dissolution stepwave model. *Science* **291**, 2400–2404.

Lasaga, A.C., Lüttge, A., 2003. A model for crystal dissolution. *Eur. J. Mineral.* **15**, 603–615.

Lasaga, A.C., Lüttge, A., 2004a. Mineralogical approaches to fundamental crystal dissolution kinetics. *Amer. Mineral.* **89**, 527–540.

Lasaga, A.C., Lüttge, A., 2004b. Mineralogical approaches to fundamental crystal dissolution kinetics-dissolution of an A_3B structure. *Eur. J. Mineral.* **16**, 713–729.

Lasaga, A.C., Soler, J.M., Ganor, J., Burch, T.E., Nagy, K.L., 1994. Chemical weathering rate laws and global geochemical cycles. *Geochim. Cosmochim. Acta* **58**, 2361–2386.

Lüttge, A., Winkler, U., Lasaga, A.C., 2003. Interferometric study of the dolomite dissolution: a new conceptual model for mineral dissolution. *Geochim. Cosmochim. Acta* **67**, 1099–1116.

Mellott, N.P., Brantley, S.L., Pantano, C.G., 2002. Topography of polished plates of albite crystal and glass during dissolution. In: Hellmann, R., Wood, S.A. (Eds.), *Water–Rock Interactions, Ore Deposits, and Environmental Geochemistry: A Tribute to David A. Crerar*. The Geochemical Society, pp. 83–95, [Special Publication No. 7].

Murakami, T., Kogure, T., Kadohara, H., Ohnuki, T., 1998. Formation of secondary minerals and its effect on anorthite dissolution. *Amer. Mineral.* **83**, 1209–1219.

Murphy, W.H., Helgeson, H.C., 1987. Thermodynamic and kinetic constraints on reaction rates among minerals and aqueous solutions. III. Activated complexes and the pH-dependence of the rates of feldspar, pyroxene, wollastonite, and olivine hydrolysis. *Geochim. Cosmochim. Acta* **51**, 3137–3153.

Nagy, K.L., Blum, A.E., Lasaga, A.C., 1991. Dissolution and precipitation kinetics of kaolinite at 80 °C and pH 3: the dependence on solution saturation state. *Am. J. Sci.* **291**, 649–686.

Nagy, K.L., Lasaga, A.C., 1992. Dissolution and precipitation kinetics of gibbsite at 80 °C and pH 3: the dependence on solution saturation state. *Geochim. Cosmochim. Acta* **56**, 3093–3111.

Oelkers, E.H., 2001. General kinetic description of multioxide silicate mineral and glass dissolution. *Geochim. Cosmochim. Acta* **65**, 3703–3719.

Oelkers, E.H., Schott, J., 1998. Does organic acid adsorption affect alkali-feldspar dissolution rates? *Chem. Geol.* **151**, 235–245.

Oelkers, E.H., Schott, J., Devidal, J.-L., 1994. The effect of aluminum, pH, and chemical affinity on the rates of aluminosilicate dissolution rates. *Geochim. Cosmochim. Acta* **58**, 2011–2024.

Schnoor, J.L., 1990. Kinetics of chemical weathering: A comparison of laboratory and field weathering rates. In: Stumm, W. (Ed.), *Aquatic Chemical Kinetics*. Wiley, New York, pp. 475–504.

Stefánsson, A., Arnórsson, S., 2000. Feldspar saturation state in natural waters. *Geochim. Cosmochim. Acta* **64**, 2567–2584.

Swoboda-Colberg, N.G., Drever, J.I., 1993. Mineral dissolution rates in plot-scale field and laboratory experiments. *Chem. Geol.* **105**, 51–69.

Tagirov, B., Schott, J., 2001. Aluminum speciation in crustal fluids revisited. *Geochim. Cosmochim. Acta* **65**, 3965–3992.

Taylor, A.S., Blum, J.D., Lasaga, A.C., 2000. The dependence of labradorite dissolution and Sr isotope release rates on solution saturation state. *Geochim. Cosmochim. Acta* **64**, 2389–2400.

Ullman, W.J., Welch, S.A., 2002. Organic ligands and feldspar dissolution. In: Hellmann, R., Wood, S.A. (Eds.), *Water–Rock Interactions, Ore Deposits, and Environmental Geochemistry: A Tribute to David A. Crerar*, Vol. 7. The Geochemical Society, pp. 3–35.

van der Hoek, B., van der Erden, J.P., Bennema, P., 1982. Thermodynamic stability conditions for the occurrence of hollow cores caused by stress of line and planar defects. *J. Crystal Growth* **56**, 621–632.

van der Salm, C., Verstraten, J.M., Tiktak, A., 1996. The influence of percolation rate on the weathering rates of silicates in an E horizon of an Umbric Albaqualf. *Geoderma* **73**, 83–106.

van der Weijden, C.H., Pacheco, F.A.L. ΔG_r dependence of weathering rates under natural conditions. *Geochim. Cosmochim. Acta* **68** Goldschmidt Abstr. Vol., A444, 2004.

Velbel, M.A., 1989. Effect of chemical affinity on feldspar hydrolysis rates in two natural weathering systems. *Chem. Geol.* **78**, 245–253.

Velbel, M.A., 1993. Constancy of silicate-mineral weathering-rate ratios between natural and experimental weathering: implications for hydrologic control of differences in absolute rates. *Chem. Geol.* **105**, 89–99.

White, A.F., 1995. Chemical weathering rates of silicate minerals in soils. In: White, A.F., Brantley, S.L. (Eds.), *Chemical Weathering Rates of Silicate Minerals*, Vol. 31. Mineralogical Society of America, pp. 407–461.

White, A.F., Brantley, S.L., 2003. The effect of time on the weathering of silicate minerals: why do weathering rates differ in the laboratory and field? *Chem. Geol.* **202**, 479–506.

Wolery, T.J. EQ3NR, A Computer Program for Geochemical Aqueous Speciation-Solubility Calculations: Theoretical Manual, User's Guide, and Related Documentation (Version 7.0). Lawrence Livermore Natl. Lab. UCRL-MA-110662 PT III, 1992.

Zhang, H., Bloom, P.R., Nater, E.A., 1993. Change in surface area and dissolution rates during hornblende dissolution at pH 4.0. *Geochim. Cosmochim. Acta* **57**, 1681–1689.

Zhu, C., Blum, A., Veblen, D., 2004. Feldspar dissolution rates and clay precipitation in the Navajo aquifer at Black Mesa, Arizona, USA. In: Wanty, R.B., Seal, R.R., IIII (Eds.), *Water–Rock Interaction WRI-11*, Vol. 1. A.A. Balkema, Amsterdam, pp. 895–899.